REVISION 1

Formation of amphibole lamellae in mantle pyroxene by fluid-mediated metasomatism: A focal plane array FTIR study from the Carpathian-Pannonian region

Nóra Liptai[1,2], Thomas P. Lange[1,3,4], Levente Patkó[1,2], László E. Aradi[3,5], Márta Berkesi[1,2], Peter M. E. Tollan[6,7], José Alberto Padrón-Navarta[8,9], Jörg Hermann[6], Szilveszter Gergely[10], Csaba Szabó[2,3], István J. Kovács[1,2]

[1] MTA FI Lendület Pannon LitH_2Oscope Research Group, Institute of Earth Physics and Space Science, Sopron, Hungary
[2] Institute of Earth Physics and Space Science, Sopron, Hungary
[3] Lithosphere Fluid Research Laboratory, Department of Petrology and Geochemistry, Institute of Geography and Earth Sciences, Eötvös Loránd University, Budapest, Hungary
[4] Doctoral School of Environmental Sciences, Eötvös Loránd University, Budapest, Hungary
[5] Present address: Department of Geosciences, University of Padova, Padova, Italy
[6] Institut für Geologie, Universität Bern, Bern, Switzerland
[7] Present address: Gübelin Gem Lab, Lucerne, Switzerland
[8] Géosciences Montpellier, CNRS-Université de Montpellier et Université des Antilles, Montpellier, France
[9] Instituto Andaluz de Ciencias de la Tierra, CSIC – University of Granada, Armilla, Spain
[10] Department of Applied Biotechnology and Food Science, Budapest University of Technology and Economics, Budapest, Hungary

Abstract

Amphiboles in the upper mantle (most frequently pargasitic in composition) have recently gained attention due to their role in the water budget and potential control on the rheology and physical discontinuity layers of the mantle. Although nominally anhydrous minerals are often analyzed with Fourier-transform infrared (FTIR) spectroscopy, amphiboles, especially in natural samples, are only scarcely in the focus of such studies because of their complex structure and variable composition. In mantle xenoliths, amphibole occurs not only interstitially or forming veins, but also as lamellae within orthopyroxene and/or clinopyroxene

grains. The genesis of such lamellae is often ambiguous, as they could either be metasomatic products, or form by exsolution without external H_2O source upon decreasing P-T conditions and consequent destabilization of hydrous point defects in the host pyroxene. To constrain the origin of amphibole lamellae in pyroxenes, we studied mantle xenoliths from the Carpathian-Pannonian region (CPR), by applying hyperspectral imaging using FTIR equipped with focal plane array (FPA) detector. Amphibole lamellae are absent in xenoliths of the central part of the CPR, but appear in those from the marginal localities which represent a well-hydrated supra-subduction mantle environment. Some of the lamella-hosting pyroxene grains are in contact with interstitial amphibole, suggesting that the formation of the lamellae is related to the amphibole-producing metasomatism; however, others have no adjacent amphibole. To determine the origin of the amphibole lamellae in pyroxenes without neighboring amphibole, the hyperspectral images were used to give an estimation of their volume proportion (0.8 – 5.1 vol.%) in the pyroxenes. Using these volume proportions, we calculated that a bulk water content of ~330-670 (orthopyroxene) and ~740-1430 (clinopyroxene) wt. ppm is needed to be contained in the host grain to be able to facilitate subsolidus exsolution of the observed amount of amphibole lamellae. These water contents are, however, too high for mantle pyroxenes, even for an aqueous-fluid saturated upper mantle. This suggests that the formation of amphibole lamellae is related to a metasomatic event with fluid input from an external water source (e.g., melt/fluid inclusion or metasomatic agent on the grain boundary).

1. Introduction

Amphibole has a wide compositional range (e.g., Hawthorne et al., 2012) and therefore can be stable in a variety of pressure-temperature conditions in crustal and upper mantle environments. In the upper mantle, amphibole dominantly has a pargasitic composition ($NaCa_2(Mg_4Al)[(Si_6Al_2)O_{22}](OH)_2$) (Hawthorne et al., 2012) and it is stable up to ~3 GPa and ~1050-1150°C (Kushiro, 1970; Green, 1973; Dawson and Smith, 1982; Niida and Green, 1999) depending on the composition (Wallace and Green, 1991; Mandler and Grove, 2016) and bulk H_2O content (Green et al., 2010; Green, 2015) of the ambient mantle. The significance of pargasitic amphibole lies in the fact that it contains up to ~ 2 wt.% of structurally bound water (as OH^-), making it one of the most significant hosts of H_2O (besides phlogopite and humite group minerals) in the upper mantle. Olivine, pyroxenes and garnet, the most modally abundant mantle minerals, are, on the other hand, all nominally anhydrous, incorporating <10-100s of wt. ppm structurally bound hydroxyl (expressed as H_2O and also

commonly referred to as water), i.e., significantly less than amphibole (e.g., Peslier et al., 2017; Demouchy and Bolfan-Casanova, 2016). It has been proposed that melting resulting from the breakdown of pargasitic amphibole where the geotherm intersects the pargasite dehydration solidus at ~3 GPa (Green et al., 2010; Kovács et al., 2017) or lower, may mark the lithosphere-asthenosphere boundary in higher heat flow areas (i.e., oceanic and young continental plates). In low heat flow (old continental) areas, the subsolidus dehydration of pargasite was suggested to be the major contributor to mid-lithospheric discontinuities (Kovács et al., 2021).

Mantle amphiboles are generally considered as products of modal metasomatism (e.g., O'Reilly and Griffin, 2013), i.e., reactions between peridotite and hydrous silicate melts or fluids, either with a subduction or intraplate origin (Coltorti et al., 2007b). Recently, experimental studies (Kang et al., 2017) proposed that amphibole formation is possible without any external H_2O source, since at high pressures the combined water content of the NAMs exceeds the amount required to form small amounts of amphibole, and decreasing P-T conditions may result in amphibole growth by dehydration of the host NAMs. Amphiboles have been widely reported in mantle xenoliths and orogenic peridotites as veins and interstitial grains, and were studied for their major and trace element composition (Coltorti et al., 2007b and references therein). However, amphibole can also be present as crystallographically-oriented lamellae in pyroxene (Smith, 1977; Isaacs et al., 1981; Veblen and Buseck, 1981) or garnet (Song et al., 2005), suggesting exsolution or replacement processes.

Fourier-transform infrared spectroscopy (FTIR) is a frequently used method to determine H_2O content and speciation in NAMs. While FTIR has also been used to analyze experimental amphiboles of different compositions (e.g., Della Ventura et al., 2003), it is rarely used to study natural amphiboles (e.g., Della Ventura et al., 2007). One distinct advantage of modern FTIR over other tools for measuring H-bearing species is the possibility to use high resolution (~6x6 μm pixel) imaging detectors, which can reveal micron-scale heterogeneities in structurally-bound H_2O (Jollands et al., 2016; Tollan and Hermann, 2019; Demers-Roberge et al., 2021) and the presence of fluid inclusions (Hidas et al., 2010; Sundvall and Stalder, 2011; Berkesi et al., 2019) or lamellae (Sundvall and Stalder, 2011).

In this paper, we present infrared spectra of natural mantle amphiboles from mantle xenoliths of the Carpathian-Pannonian region, and compare them with previously published amphibole spectra. Furthermore, we introduce how FTIR hyperspectral imaging can be used to characterize the appearance and distribution of hydrous (amphibole) lamellae in pyroxenes.

The results are then used to quantify H_2O contents and deduce their origin, namely whether they could form by exsolution from pyroxene or by introduction of a metasomatic fluid. We also provide a brief summary how much uncertainty is present in the quantitative unpolarised estimations for the amphibole proportions arising from the thickness and orientation of amphibole lamellae in the host pyroxenes.

2. Previous FTIR studies on pargasitic amphibole and amphibole lamellae

Natural mantle amphiboles, although often analyzed for their geochemical composition to characterize metasomatic agents, are seldom the focus of quantitative FTIR studies, because the chemical complexity and high water contents make it difficult to determine calibration factors such as with NAMs. Della Ventura et al. (2007) studied natural pargasitic amphiboles from a metasomatized spinel peridotite from Lherz, concluding that FTIR can be used to detect O^{2-} in certain chemical conditions (lack of F^- and significant amounts of Fe^{2+}). Spectrum fitting applied by the authors suggested that the anion composition at the O3 (anionic) site is likely occupied by OH^- and O^{2-} in equal proportion. The abundance of O^{2-} at the O3 site is resulting from dehydrogenation and is correlated with the amount of Fe^{3+} and Ti^{4+} as concluded from observations on other natural amphiboles (Ernst and Wai, 1970; Phillips et al., 1989; Popp et al., 1995).

FTIR is often used as one of the tools to constrain short range order of cations and anions in the amphibole structure (e.g., Della Ventura et al., 1999; Robert et al., 1999; Day et al., 2018), by fitting component peaks on the spectrum which correspond to different configurations (i.e., the cations surrounding the anion at the O3 site). However, this is challenging to carry out on natural amphiboles due to their more complex chemical composition, which yields more bands in the principal OH-stretching region, making spectrum fitting more difficult (Heaveysege et al., 2015). Because of this, available infrared spectroscopic data on pargasitic amphibole mainly involves studies on gem quality pargasites with simpler chemical composition (e.g., Heaveysege et al., 2015; Day et al., 2018), in addition to synthetic pargasite. FTIR spectra of experimentally synthesized pargasites are used to characterize the OH-F substitution (Robert et al., 2000; Della Ventura et al., 2001), and the change of absorption bands and configuration groups over the chemical transition to other compositions such as richterite (Della Ventura et al., 1999), tremolite (-cummingtonite) (Della Ventura et al., 2003; Jenkins et al., 2003; Ishida et al., 2008) and Cr-pargasite (Fialips-Guédon et al., 2000).

Several works report absorption bands of amphibole (pargasite) appearing on the infrared spectra of other mantle minerals, dominantly pyroxenes. Absorption bands at high wavenumbers (~3675 cm^{-1}) were clearly distinguished from those of pyroxenes and attributed to amphibole lamellae (Ingrin et al., 1989; Skogby and Rossman, 1989). Skogby et al. (1990) reported infrared spectra showing amphibole lamellae in ortho- and clinopyroxenes from a wide range of geological environments, although amphibole was not detected in mantle-derived samples. The authors also proposed that FTIR is a suitable method to detect the presence of sub-microscopic amphibole lamellae at levels of 5 unit cells in thickness under favorable conditions. Andrut et al. (2003) found amphibole lamellae in a diopside single crystal, and concluded that they formed under high water activity during crystallization. Sundvall and Stalder (2011) described amphibole lamellae identified by FPA-FTIR imaging around cracks within natural orthopyroxene. Experimental studies of Green et al. (2010) and Kovács et al. (2012) aimed to constrain the activity and distribution of H_2O between NAMs and hydrous mantle phases (pargasite and phlogopite) in lherzolite at pressures of 2.5 and 4 GPa. At the lower pressures, in accordance with the ~3 GPa upper stability limit, absorption bands of pargasite appeared on the FTIR spectra of the lherzolite matrix (Kovács et al., 2012). Absorption bands around 3600 cm^{-1} in synthetic enstatite were also interpreted to result from the presence of amphibole lamellae (Rauch and Keppler, 2002), however, this is significantly lower than the wavenumber range typically exhibited by amphibole (Della Ventura et al., 1999; 2003; 2007).

3. Upper mantle amphiboles of the Carpathian-Pannonian region

The Carpathian-Pannonian region (CPR) is located in Central Europe and includes an extensional basin system surrounded by the Carpathians, Alps, and Dinarides. Upper mantle xenoliths are hosted in late Miocene – Pleistocene alkali basalts in five localities (Fig. 1), including Styrian Basin and Perşani Mountains on the western and eastern margins, respectively, and Bakony-Balaton Highland, Little Hungarian Plain and Nógrád-Gömör in the central areas. The CPR has a complex Cenozoic tectonic history (see Horváth et al., 2015 for a review). Followed by the juxtaposition of two microplates, AlCaPa and Tisza-Dacia, the region was subjected to significant extension (i.e., lithospheric thinning) and coupled asthenosphere upwelling aided by subduction rollback on the eastern margin during the early to late Miocene. After the cessation of the extension, large-scale tectonic inversion (compression attributed to the push of the Adria microplate) dominated the region, and the

xenolith-hosting alkali basalts erupted during this period (Kovács et al., 2020 and references therein). The xenolith localities in both the western and eastern margins represent a hydrated, supra-subduction mantle environment (Aradi et al., 2017; Faccini et al., 2020), whereas the central area is characterized by a dry and rigid lithosphere strongly affected by the extension (Patkó et al., 2019; Liptai et al., 2021). This is reflected in the water contents of their NAMs: olivine, orthopyroxene and clinopyroxene have H_2O contents of 3-15 84-305 and 186-674 wt. ppm, respectively, in the marginal areas (Falus et al., 2008; Aradi et al., 2017) and 0-4, 0-114, and 3-481 wt. ppm, respectively, in the central areas (Patkó et al., 2019; Liptai et al., 2021). The CPR can be utilized as an excellent area to study the behavior of hydrous (metasomatic) minerals in an inverted extensional basin, where the extension only ceased ~10 Ma ago and the inversion is still ongoing. The recent (<8 Ma) transport of the xenoliths to the surface provides an exceptional insight into the probably still active lithospheric processes, such as the formation and break-down of hydrous minerals.

Amphiboles were reported in small modal proportions as interstitial grains in several peridotite xenoliths (e.g., Kurat et al., 1980; Downes et al., 1992; Szabó and Taylor, 1994; Bali et al., 2002; Coltorti et al., 2007a; Aradi et al., 2017; Créon et al., 2017; Liptai et al., 2017), and as both veins and interstitial grains in some xenoliths from the Perşani Mountains (Vaselli et al., 1995; Faccini et al., 2020). Higher modal proportions appeared in a few amphibole-rich samples in the Styrian Basin (>13 vol.%; Aradi et al., 2017), metasomatized cumulates underplating the Moho in the Nógrád-Gömör (Kovács et al., 2004), and rare composite xenoliths containing amphibole-rich parts, interpreted as veins, in the Bakony-Balaton Highland (Embey-Isztin, 1976; Bali et al., 2018). In the peridotites of both the Nógrád-Gömör and the Perşani Mountains, two generations of amphiboles were distinguished based on their high field strength element contents (Liptai et al., 2017; Faccini et al., 2020). In the Styrian Basin, amphiboles have formed at various distances from a metasomatic front of a hydrous mafic melt assumed to have a nephelinitic source (Aradi et al., 2020). In the Bakony-Balaton Highland, the small amount of interstitial amphiboles were found to have formed via interaction with a hydrous silicate melt (Créon et al., 2017), and the amphibole-rich vein described by Bali et al. (2018) is proposed to have crystallized from a melt derived from alkali basalt by high degree fractionation.

In the CPR, petrographic evidence of amphibole lamellae within pyroxenes have only been reported in metasomatized, amphibole-rich xenoliths from the Styrian Basin (Aradi et al., 2020). On the other hand, absorption bands in the wavenumber range of 3675-3710 cm^{-1} were found in pyroxene spectra both in the Styrian Basin (Aradi et al., 2017) and the Nógrád-

Gömör (Patkó et al., 2019), which were both attributed to the presence of sub-microscopic lamellae of pargasitic amphibole.

4. Sampling and analytical methods

4.1. Sample selection and description

We selected 34 xenoliths (9, 5, 16 and 4 from the Styrian Basin, Bakony-Balaton Highland, Nógrád-Gömör and Perşani Mountains, respectively) for detailed investigation of sub-microscopic amphibole lamellae in pyroxenes by means of hyperspectral mapping and imaging, in addition to obtaining single infrared spectra of individual amphibole grains. The samples were studied in detail previously, focusing on their geochemistry (Liptai et al., 2017; Aradi et al., 2020), crystal preferred orientation (Aradi et al., 2017; Liptai et al., 2019) and H_2O contents in NAMs (Aradi et al., 2017; Patkó et al., 2019; Liptai et al., 2021). The four Perşani Mountains xenoliths are from the sampling site 'Gruiu' (see Fig. 1 of Falus et al., 2008) and were not analyzed before; two are lherzolites (PGR-X1-0306, PGR-X1-0347), one is a lherzolite with a crosscutting amphibole vein (PGR-X2-0396) (Fig. 2a) and one is an amphibole wehrlite (PGR-14182). Xenoliths from the Styrian Basin and Perşani Mountains, which are assumed to represent supra-subduction mantle portions, all contain amphibole as interstitial grains (Fig. 2b). On the other hand, xenoliths from the Bakony-Balaton Highland and Nógrád-Gömör, which originate from the central areas of the Pannonian Basin, are dominantly amphibole-free except for a few grains. These often appear as remnants in the core of melt pockets (Fig. 2c) suggesting that their lower abundance is due to breakdown at high temperatures (Liptai et al., 2017).

Geochemical data are available for the amphiboles in xenoliths included in this study from the Styrian Basin (Aradi et al., 2020) and Nógrád-Gömör (Liptai et al., 2017). In the Nógrád-Gömör, part of the interstitial amphiboles showed low Nb-content (NMS1304, NMS1308, NFL1329; Table 1), interpreted to be remnants of a subductional metasomatic event preceding the formation of the CPR, although the pyroxenes within the same xenoliths showed no sign of cryptic metasomatism (except for NMS1304). The other part of the amphiboles, with high Nb-content, were interpreted to be associated with younger, intraplate basaltic melt infiltrations, causing the enrichment of various trace elements, such as U, Th and rare earth elements in both amphiboles and pyroxenes (Liptai et al., 2017). In the Styrian Basin, amphiboles in the xenoliths represent metasomatic products at increasing distances

238 from a nephelinitic melt channel and showing different geochemical characteristics
239 accordingly. The closest domain (GN1407) shows enrichment in LREE, K, U-Pb, Nb-Ta and
240 a strong impact of fluid metasomatism. Further away from the channel (BEI1401, GN1401,
241 GN1411, TOB1401) amphiboles have decreasing LREE and Nb-Ta concentrations, and in the
242 distal domain (GN1406, GN1412, PST1401, PST1403, TOB1403) there are only minor
243 amphiboles growing on clinopyroxenes and mimicking their trace element distributions
244 without the enrichment of fluid mobile elements. Unpublished data from two Perşani
245 Mountains amphiboles show different geochemical characteristics: PGR-X1-0347 has low
246 LREE and HFSE contents, whereas both interstitial and vein amphiboles in PGR-X2-0396 are
247 enriched in these elements.
248 Sample selection was carried out with the goal of having a wide variety of xenoliths
249 analyzed (amphibole-hosting and amphibole-free, geochemically depleted and metasomatized
250 where such data was available), to find any potential systematics in the appearance of
251 amphibole lamellae. In a few pyroxene grains in xenoliths from the Styrian Basin and Perşani
252 Mountains, amphibole lamellae were observable in optical microscope; in one clinopyroxene,
253 they appeared together with spinel inclusions (Fig. 2d), which have been previously described
254 in Styrian Basin xenoliths (Aradi et al., 2020). However, because previous studies (e.g., Patkó
255 et al., 2019) have found evidence of hydrous lamellae on the FTIR spectrum of pyroxenes
256 even though it was not visible in optical microscope, we included clear-looking grains for our
257 analyses as well.Besides the lamellae-hosting pyroxenes, we analyzed amphibole crystals
258 both as interstitial grains in the xenolith thick sections, and as grains separated by hand-
259 picking from the xenoliths. In the latter case, 7-8 grains were separated from one xenolith of
260 the Styrian Basin (GN1407) and the Perşani Mountains (PGR-14182) each, with the aim of
261 comparing their spectra with those of the lamellae.
262
263 **4.2. FTIR spectroscopy and single point mapping**
264 Acquisition of amphibole single spectra from the separated grains was carried out using
265 a Perkin Elmer Spectrum 400 infrared spectrometer and a coupled Spotlight 400 FTIR
266 imaging system at the Budapest University of Technology and Economics. Hyperspectral
267 maps were obtained on double-polished thick (95-760 μm; Table 1) sections using a Bruker
268 FTIR Vertex 70 spectrometer equipped with a Globar light source and MCT-A detector,
269 coupled to a Bruker Hyperion 2000 microscope at the Institute for Geological and
270 Geochemical Research, Budapest. Infrared spectra both in single spot analyses and

hyperspectral maps were acquired with unpolarized light, in the spectral range of 4000-400 cm^{-1}, with a spectral resolution of 4 cm^{-1}, and 128 scans were accumulated for both the background and the samples. Individual analyses of amphibole grains were carried out with an aperture size of 100x100 or 50x50 µm depending on the grain size and clarity. For the acquisition of the single spot hyperspectral maps, we used a 50x50 µm aperture, and a step size of 30 to 40 µm to have some overlap. Depending on the pyroxene grain size, the maps consisted of grids of 5x5 to 10x10 points of single spot spectra. Background with the according aperture size was collected after every 10-18 spectra. To analyze the spectra and assemble hyperspectral maps, we used the OPUS® software. Baseline correction was applied on all spectra using the concave rubberband correction routine with two iterations and 64 baseline points. The hyperspectral images are based on the integrated absorbances in the analyzed spots, which were obtained by integrating in a wavenumber range fully including the bands of the hydrous phases (usually between ~3750-3650 cm^{-1} depending on the grain). The linear baseline of the integrated area was defined by the intensity values at the starting and endpoint of the integration range ('B' type integration in OPUS).

For the amphibole single point spectra to be quantitatively comparable with the lamellae, i.e., to accurately represent water content, two issues need to be resolved. First, absorbance intensity is not linearly correlated with H_2O content in bands exceeding an intensity of ~0.2-0.3 linear absorbance units (Libowitzky and Rossman, 1997), which is usually the case in thick sections of several hundred µm, such as the xenoliths in this study. To acquire spectra with maximum absorbances below this value, separated amphibole grains were embedded in Crystalbond™ and thinned to as low as 30-80 µm. Second, because amphibole is anisotropic, its absorbance intensity varies depending on the crystallographic orientation with respect to the infrared beam. Therefore, we obtained spectra from 7-8 separated amphibole grains per sample, which were unoriented during impregnation. The thickness-normalized average of these spectra can then be considered as a reasonable estimation to minimize the uncertainty arising from anisotropy.

4.3. FPA-FTIR imaging

FPA-FTIR imaging on selected samples (Table 1) was carried out using a Bruker Tensor 27 spectrometer with a Globar infrared source coupled to a Bruker Hyperion 3000 microscope at the University of Bern. These analyses were performed in a sample chamber with a dry air purge. The detector used was a focal plane array (FPA) detector, which is

capable of collecting 4096 (64x64) spectra simultaneously within a fixed size grid (170x170 μm). Depending on the size and shape of the analyzed grains, up to 6 grids in both dimensions were stitched together to create composite images. To reduce analysis time, resolution was set to 8 cm^{-1} and the number of accumulated scans to 64 following testing and confirming that it does not significantly reduce spectrum quality. We used a 2x2 binning to increase signal to noise ratio and to reduce the output file size, which resulted in a nominal resolution of approximately 5.4 μm. Baseline was corrected in all acquired spectra, with the same software (OPUS) and method as with the FTIR mapping (rubberband correction routine with two iterations and 64 baseline points). Integration was carried out by the same principles as described above at the single point mapping.

4.4. Estimating quantitative uncertainties: the role of orientation and thickness of amphibole lamellae

The absorption of infrared light in the OH-region of amphiboles is strong and the absorption indicatrix is rather anisotropic (almost no absorption along two principal polarized axes; Skogby and Rossman, 1991). Therefore, it is important to estimate the impact of these two factors on unpolarized absorbance. It is known that unlike polarized absorbance, unpolarized absorbance is not linearly proportional to thickness if the absorption is strong (i.e. thicker sections) or the anisotropy is large (e.g. as for amphiboles) (Libowitzky and Rossman, 1996). Nevertheless, it is possible to predict accurately the unpolarized absorbance in a given indicatrix section based on polarized measurements using the infrared absorption indicatrix theory in the transmission domain (Kovács et al., 2008; Sambridge et al., 2008; Withers, 2013; Qiu et al., 2018). For this purpose, we digitalized the three principal polarized infrared spectra of a sodian cummingtonite showed in Fig. 1 of Skogby and Rossman (1991). The published spectra are displayed at 1 μm of thickness. To demonstrate the effect of thickness and anisotropy on the unpolarized absorbance, we calculated the principal polarized, average, minimum and maximum unpolarized spectra at 1, 10 and 60 μm of thickness (Fig. 3). Although sodian cummingtonite is used for the calculations based on Skogby and Rossman (1991), the absorption indicatrix of chemically different amphiboles does not differ significantly. The principal polarized spectra were scaled simply with thickness, whereas the maximum and minimum unpolarized spectra were computed using equations 2 and 8 in Libowitzky and Rossman (1996). The average unpolarized spectra were calculated from principal polarized transmittances as given by Equation 15 in Withers (2013). While the polarized absorbances increase proportionally with thickness, the unpolarized absorbances,

338 especially the minimum and average, do not change proportionally with thickness, which is
339 especially evident for the 60 μm thick section (Fig. 3). Since the unpolarized reference spectra
340 that is used later in this work to estimate the proportion of amphibole lamellae in pyroxenes
341 were recorded on wafers which are ~60 μm on average, the amount of underestimation with
342 respect to the true total polarized absorbance can be calculated. For this purpose, we
343 determined the integrated area under both polarized and unpolarized spectra (Table 2) and
344 compared the total polarized integrated absorbance to three times the average, minimum and
345 maximum unpolarized absorbance (Kovács et al., 2008; Withers, 2013), from which we can
346 estimate how much we underestimate the actual amphibole content based on the measured
347 unpolarized spectra. It is evident that with increasing thickness the correction factors for the
348 average and the minimum unpolarized absorbances increase, meaning that the total polarized
349 absorbance is more and more underestimated. Naturally the correction factors for the
350 minimum and maximum absorbances are the highest and lowest, respectively. The correction
351 factor for the minimum absorbance in principle does not change with thickness, as this section
352 is isotropic where there is only weak absorbance, therefore the unpolarized absorbance
353 changes linearly with thickness over a wider range of absorbances. As shown in Table 2, the
354 correction factor at 60 μm thickness for the average, minimum and maximum unpolarized
355 absorbance are 1.68, 4.6 and 1.26 respectively. It can be modelled from Equation 15 in
356 Withers (2013), assuming that the direction of the incident light with respect to the indicatrix
357 is unoriented and equally distributed on a sphere, that most of the absorbance would vary in a
358 relatively narrow range around the average unpolarized absorbance and only a few, if any
359 measured, would be close to the maximum or minimum values. This is also in agreement with
360 the spectra we measured on unoriented amphibole sections (see Results section 5.1).
361
362 **5. Results**
363
364 **5.1. Amphibole single spectra**

365 Due to the scarcity, small size and lack of clarity of interstitial amphiboles in the
366 selected xenoliths, only a few good quality spectra could be collected which were free of
367 contamination from nearby grain boundaries. Examples of unoriented single-grain amphibole
368 spectra from all four localities are depicted on Fig. 4a-b, compared with unpolarized single-
369 crystal spectra of Ti-rich and synthetic pargasites published by Della Ventura et al. (2007).
370 The positions of the main absorption bands in the amphiboles in this study appear at ~ 3706,

3680 and 3656 cm^{-1}, which is in good agreement with the Ti-rich pargasite from Lherz (3710, 3686, and 3660 cm^{-1}). However, the intensities of these bands are different: in the Nógrád-Gömör and Perşani Mountains samples, the highest intensity band is the one at 3680 cm^{-1}, followed closely by the one at 3706 cm^{-1}, whereas the third band at 3656 cm^{-1} is not present or with only minimum intensity. In the spectrum of the amphibole from the Bakony-Balaton Highland, the third band (3656 cm^{-1}) is the most intense, and in the sample from Styrian Basin, the second and third bands (3680 and 3656 cm^{-1}) are similar in intensity and the band at 3706 cm^{-1} is slightly lower. Note that these example spectra were taken from one grain each due to the small number of amphiboles that could be qualitatively analyzed (1-2 per sample), therefore they cannot be used for quantitative interpretation as they represent only one random orientation.

The amphibole spectra collected from distinct grains of the vein in xenolith PGR-X2-0396 (Fig. 2a) also show some variability in shape (Fig. 4c), with either the band at 3680 or 3656 cm^{-1} showing the highest intensity. In contrast, the amphibole spectra collected from randomly oriented separated grains from a Perşani Mountains and a Styrian Basin xenolith (Fig. 4d, e, respectively) show homogeneous band positions and spectrum shapes. Although maximum absorbance intensities have a great variance (between ~40-45 and ~13-14 when normalized to 1 cm), they cover the same range in both samples, indicating that the measured crystallographic orientations cover well the absorbance indicatrix. The relative intensities of the bands are different in the two samples: in the Styrian Basin, the bands at 3710 and 3686 cm^{-1} have similar intensities but the one at ~3656 cm^{-1} is not distinguishable, whereas in the Perşani Mountains sample, the band at 3686 cm^{-1} shows the highest absorbance while the other two are significantly smaller. The shapes of the spectra and the relative band intensities are identical within samples, which indicates that this may depend on composition rather than orientation.

5.2. Hyperspectral maps

FTIR hyperspectral mapping and imaging revealed the presence of hydrous phases in ortho- or clinopyroxenes in 18 xenoliths (Table 1). Absorption bands of these hydrous components appear in a slightly higher wavenumber range than the OH-absorption range of pyroxenes (i.e., >3630 cm^{-1}), at three characteristic positions at ~3712-3708, ~3696-3694, and ~3686-3678 cm^{-1} (Fig. 5), with an additional rare band appearing at ~3625 cm^{-1} in orthopyroxene in two samples (Table 1). In some xenoliths, the bands around 3710 and 3680

404 cm^{-1} both appear on the spectra of the same grain (Fig. 5a), which corresponds to the major
405 absorption bands of pargasitic amphibole (Della Ventura et al., 2007). On the other hand, the
406 one at ~3695 cm^{-1} only appears as a single band (Fig. 5b), except in the two samples where it
407 is accompanied by a band at ~3625 cm^{-1} (distinguishable only in orthopyroxene). The
408 identification of these bands is discussed below in section 6.1.
409 Hyperspectral maps and images were constructed by integrating absorbance in each
410 measurement point, in the wavenumber range characteristic for the hydrous phases (around
411 3740-3630 cm^{-1}, varying in each sample). In general, the single point FTIR map reveals the
412 presence of hydrous phases within a grain; however, FPA-FTIR imaging shows their exact
413 locations and distribution, and different intensities could be well distinguished (Fig.6). The
414 distribution of hydrous phases is variable, in some images they are broadly distributed
415 throughout the crystal, whereas in others, they are more locally concentrated in smaller sub-
416 crystal regions. Phases with absorbance bands appearing at ~3710 and ~3680 cm^{-1} always
417 show elongated, parallel, lamella-like shapes (Fig. 6, 7a), whereas those with bands at ~3695
418 and ~3625 cm^{-1} have irregular shapes, and are often linked to intragranular cracks or grain
419 boundaries (Fig. 7b). The lamellae can sometimes be observed with optical light as well (e.g.,
420 Fig. 6), but the distinction from clinopyroxene lamellae in orthopyroxene (or vice versa) is not
421 straightforward. In two samples, FPA-FTIR images revealed single hydrous lamellae within
422 orthopyroxenes which also contain most likely clinopyroxene lamellae based on the optical
423 microscopic images (Fig. 7c, 7d). Note that in such cases, small proportion of amphibole may
424 not be detectable next to the clinopyroxene signal. In xenoliths from the Perşani Mountains,
425 lamellae appear in pyroxene grains directly adjacent to interstitial amphibole (Fig. 7e, f), and
426 a decrease could be observed in the density of lamellae towards the core of the grain (Fig. 7f).
427 In these samples, infrared spectra show mixture of amphibole and pyroxene, and the intensity
428 of absorbance bands characteristic for amphibole gradually decrease towards the core where
429 they are no longer detectable (Fig. 8).
430 To quantify the water content of bulk grains by spectrum mixing (see section 6.2), the
431 water contents of host pyroxenes were calculated using spectra of lamella-free pyroxene parts
432 from the hyperspectral images in two samples (PGR-X1-0306 and GN1406) where previous
433 data on pyroxene water content was not available. To calculate the water content from the
434 infrared spectrum, we used the calibration factors of Bell et al. (1995) and followed the
435 method described step-by-step in Patkó et al. (2019). Note that when calculating water
436 content, even one unoriented grain can give sufficient accuracy (Xia et al., 2013). The

resulting water contents for the PGR-X1-0306 orthopyroxene and GN1406 clinopyroxene (Fig. 6) are 166 and 506 ppm, respectively.

6. Discussion

6.1. Identification of the hydrous phases

One of the greatest advantages of hyperspectral mapping and imaging is that it offers a combination of phase identification and their 2D distribution, hence the wide usage to map or image H_2O-related heterogeneities such as fluid inclusions or hydrogen diffusion. However, hydrous lamellae were so far only rarely studied by hyperspectral mapping and imaging (Sundvall and Stalder, 2011). Amphibole lamellae, while possibly observable with polarized light microscopy, are often not well distinguishable from other pyroxene lamellae (i.e., clinopyroxene lamellae in orthopyroxene or vice versa) (Fig. 7d). Hyperspectral imaging not only aids identification, but also reveals the distribution of such lamellae. Pyroxene lamellae usually have a homogeneous distribution within the host pyroxene grain, because they form by subsolidus exsolution; however, in our samples, FPA imaging revealed a heterogeneous distribution of the lamellae (Fig. 7a, e, f), which poses the question of formation mechanism. Furthermore, the resolution of the FPA detector allowed the detection of smaller lamellae (few μm or smaller across), where the volume ratio of the lamella and the host is so little that single spot FTIR analysis, which samples a greater volume, would not be able to detect it.

Bands of the hydrous phases appearing on the pyroxene spectra of the hyperspectral maps at ~3712-3708 and ~3686-3678 cm^{-1} correspond to those observed in pargasite (Della Ventura et al., 2007) and in the amphibole single spectra of this study (Fig. 4). The shapes of these phases always appear as lamellae. On the other hand, the phases with bands at ~3695 and ~3625 cm^{-1} have irregular shapes and often follow grain boundaries, which suggests it being a secondary phase.

Pyroxene and olivine are commonly known to be susceptible to being replaced by hydrous minerals, such as serpentine (e.g., Moody, 1976) if slow exhumation facilitates re-equilibration at lower pressures, as observed in oceanic and orogenic peridotites. High-temperature serpentine (antigorite) may form *in-situ* in the hydrated mantle, if the temperature does not exceed ~700°C at 2 GPa (Ulmer and Trommsdorff, 1995; Padrón-Navarta et al., 2010), for instance in cratonic areas underlain by a subducted slab (e.g., Facer et al., 2009). However, in intraplate alkali basalt-hosted xenoliths, where the sampled mantle portion is

warmer (usually >900°C), and transport to the surface can be considered instantaneous on the geological time scale, conditions for *in-situ* serpentinization are unlikely.

FTIR spectra of serpentine minerals have absorption bands in the OH-region at wavenumbers close to what our analyses revealed (Fig. 5b): chrysotile at 3693 and 3647, and lizardite at 3687 and 3644 cm^{-1} (Madejová et al., 2017). Gose et al. (2011) presented FTIR spectra of serpentinized orthopyroxene to investigate water loss in oceanic peridotite. The serpentine signal looks very similar to those on some of the pyroxene spectra from the Finero peridotite (Tommasi et al., 2017 and unpublished data). However, in these studies, the absorption bands are significantly wider, and the wavenumber position of the second, smaller band is different compared to the ones in our results (~3695 and 3625 cm^{-1}). Therefore, we suggest that these absorption bands in our samples do not correspond to serpentine minerals. Clay minerals which are common weathering products of pyroxenes on the surface (kaolinite, smectites; Noack et al., 1993), are better candidates. Some kaolin-group minerals have absorption bands at ~3700-3694 and ~3628-3620 cm^{-1} (Madejová et al., 2017). Furthermore, as the hyperspectral images suggested that these phases appear at or near grain boundaries and cracks (Fig. 7b), small amounts of iddingsite replacing the adjacent olivine cannot be excluded either. It is worth noting that in the previous FTIR study on Nógrád-Gömör xenoliths (Fig. 1), absorption bands at various wavenumber positions between ~3697-3672 cm^{-1} (and in a few orthopyroxenes, at ~3630 cm^{-1}) were reported (Patkó et al., 2019), and were attributed to hydrous lamellae, most likely amphibole. While some bands (likely between ~3685-3675 cm^{-1}) may indeed be amphibole, we suggest that bands at higher wavenumbers (~3697-3690 cm^{-1}) are more likely to be secondary weathering products, especially if accompanied by another band at ~3625 cm^{-1}.

6.2. Proportion and genesis of the amphibole lamellae

The main question regarding the amphibole lamellae is whether or not they could have formed solely by exsolution within the pyroxenes through re-distribution of the H_2O stored in the host pyroxene lattice defects. In a young (off-cratonic) continental environment with high heat flow, the upper limit of the stability of pargasitic amphibole is controlled by temperature rather than pressure (Kovács et al., 2021). Pargasite becomes stable at ~1100°C or even lower temperatures in a depleted mantle environment (Wallace and Green, 1991). During the tectonic history of the CPR, a significant decrease in temperature is assumed to have happened, following the extension and asthenosphere up-doming in the Miocene (e.g.,

Horváth, 1993), which could have facilitated sub-solidus amphibole exsolution in pyroxenes. However, as Patkó et al. (2019) proposed in their study on NAMs from the Nógrád-Gömör, extension and the coupled decompression in the thinning lithosphere resulted in a significant degree of H_2O loss in both ortho- and clinopyroxene. Therefore, although post-extensional cooling may have provided the temperature conditions needed for amphibole exsolution, the decompression-induced dehydration likely had an opposing effect, greatly reducing the availability of H_2O for amphibole lamellae exsolution. This does not exclude amphibole formation at the grain boundaries (interstitially).

In one of the xenoliths from the Perşani Mountains (PGR-X1-0347), interstitial amphibole is adjacent to the grains targeted with the FPA-FTIR imaging (Fig. 7e, f). In the case of the orthopyroxene (Fig. 7f), the amphibole lamellae clearly start at the grain boundary from the direction of the amphibole, and the amphibole signature becomes weaker on the infrared spectrum before completely disappearing towards the core of the orthopyroxene grain (Fig. 8). In fact, in the upper right part of the hyperspectral image (spot nr. 4-5 on Fig. 8), the infrared spectrum is a mixture of amphibole and orthopyroxene, which is likely due to the overlapping of the two grains rather than lamellae. In the case of the clinopyroxene neighbored by an interstitial amphibole (Fig. 7e), this 'infiltration' phenomenon is less obvious, as the lamellae appear in the core as well, but the mechanism is likely the same. This may also be supported by the greater similarity of the amphibole crystallographic properties to that of the clinopyroxene compared to orthopyroxene.

To determine whether water content of the pyroxenes would be sufficient for sub-solidus amphibole formation, we need to estimate the proportion of amphibole in the grain and calculate the amount of excess H_2O (beyond what is normally held in pyroxene) needed for lamella formation. For this, using the amphibole 'shoulder' on the pyroxene spectra (between ~3740-3640 cm^{-1}) in the hyperspectral image, the contribution of the amphibole lamella to the total OH band can be estimated in volume percent. We chose the orthopyroxene grain in the Perşani Mountains xenolith PGR-X1-0306 (Fig. 7a) for two reasons: (1) there is no adjacent interstitial amphibole observable by optical microscopy which could act as a source, and (2) the absorption bands of amphibole are more easily distinguishable on the orthopyroxene spectrum, as the OH-stretching region of water incorporated in orthopyroxene is at lower wavenumbers.

We applied spectrum mixing, using cm-normalized spectra of a lamella-free orthopyroxene and amphibole spectra obtained from the separated amphibole grains to model the different volume proportions of amphibole. We chose the Perşani Mountains amphiboles

(Fig. 4c) because of a better fit in terms of spectrum shape (the band at 3686 cm^{-1} being the highest). Based on the hyperspectral images, we distinguished three groups with different amount of amphibole presence. We redrew the image with these groups indicated with different colors for easier calculation of area percentages (Fig. 9a). The dark blue ('dry'), light blue (low amphibole) and green (high amphibole) areas make up ~ 75, 22 and 3 % of the map, respectively (Table 3). Since lamellae orientations are unknown, we applied the mixing with both the maximum and minimum absorbance amphibole spectra, as well as the sample average. The resulting mixed spectra with varying amphibole content are shown on Fig. 9b-d in grey color. Since a spectrum represents information on the whole thickness of the section, the area percentages on the hyperspectral maps may be considered equivalent to volume percentages. Note that the FPA-FTIR image does not cover the whole grain and the lamellae are not distributed homogeneously, however, since there are more lamellae towards the lower right part and they are more absent toward the upper left (Fig. 9a), we consider it as an acceptable representation of the grain.

Using the amphibole spectrum with the highest absorbance for mixing (Fig. 9b), the above distinguished areas (dark blue, light blue and green on Fig. 9a) correspond to 0, 5, and 10 vol.% amphibole (Table 3), respectively. Applying mass balance calculation, this amounts to 1.40 vol.% amphibole content, equaling to 1.37 wt.% (the difference is negligible). Mixing with the lowest absorbance amphibole spectrum, the three areas represent 0, 15, and 35 vol.% amphibole (Fig. 9c), which adds up to 4.35 vol.% (4.25 wt.%) amphibole content using mass balance calculation. Note that the fit of the spectra may be imperfect as the shape of the mixed spectrum depends on the shape and relative intensities of bands in the amphibole spectrum used for the mixing. Using the averaged amphibole spectrum for the mixing (Fig. 9d), which can likely be considered as the most realistic scenario, the lamella-hosting areas result in having 10 and 20 vol% amphibole content, equaling to a total of 2.80 vol.% (2.73 wt.%) amphibole in the bulk analyzed area (Table 3).

As mentioned in section 4.4, these obtained amphibole proportions are overestimations, meaning that seemingly more amphibole is needed to account for the observed absorbances in the 3600-3750 cm^{-1} range than what is actually present. Therefore, it is necessary to use the determined correction factor to estimate the more realistic values. Since the correction factor should be less with decreasing thickness (note that the reference spectra used for spectral mixing are recorded at ~60 μm) the correction factor would provide only minimal estimates for the proportions of amphiboles in pyroxenes. Dividing the obtained amphibole proportions with the average correction factor for 60 μm (1.68; Table 2) resulted in amphibole ratios of

571 0.83, 2.59 and 1.67 vol.% (0.81, 2.53 and 1.63 wt.%) for the mixing with the highest, lowest,
572 and average amphibole spectra, respectively (Table 3). Note that the correction factor may
573 also be applied before spectrum mixing (i.e., on the pure amphibole spectrum used for the
574 mixing), to get the same corrected amphibole proportions.

575 The next step is to assess whether the pre-exsolution (parental) orthopyroxene could
576 have contained enough H_2O to explain the calculated volume of exsolved amphibole. As
577 calculated above based on its infrared spectrum, the host orthopyroxene contains 166 ppm
578 H_2O, and the proportion of the amphibole lamellae is between 0.81 – 2.53 (on average, 1.63)
579 wt.%. Assuming 2 wt.% H_2O in the amphibole (based on pure pargasite composition), a H_2O
580 content of 162-506 (on average, 326) ppm would have had to be present in the parental
581 orthopyroxene to generate the calculated amount of exsolved amphibole. Taking into account
582 the measured H_2O concentration in the host orthopyroxene (166 ppm), the total H_2O
583 concentration of the parental orthopyroxene must have been 327-668 (on average, 489) ppm
584 (see breakdown of calculation in Table 3). In the continental off-cratonic upper mantle, the
585 content of orthopyroxenes is normally around 100-200 ppm and very rarely exceed 400 ppm
586 (Peslier et al., 2017; Demouchy and Bolfan-Casanova, 2016), and orthopyroxenes in the
587 supra-subduction Styrian Basin and Perşani Mountains have similar values, with only a few
588 samples having orthopyroxene water contents above 200 ppm (Falus et al., 2008; Aradi et al.,
589 2017). It is unlikely that orthopyroxene in a young continental environment could exsolve this
590 amount of amphibole unless exceptionally hydrated. However, the smaller the amphibole
591 proportion is, the less likely it can be detected with FTIR. For example, 100 ppm H_2O would
592 be sufficient for 0.5 wt.% of amphibole, which would need to be localized into a few bigger
593 lamellae to be able to be detected. In the imaged orthopyroxene of xenolith PST1401 (Fig.
594 7d), the single amphibole lamella may in fact be accompanied by others which are below
595 detection.

596 Clinopyroxene, on the other hand, may hold about 2-3 times as much H_2O as
597 orthopyroxene, up to 500-600 ppm (Peslier et al., 2017; Demouchy and Bolfan-Casanova,
598 2016). In principle, clinopyroxene would be able to exsolve ~1-1.5 % amphibole (200-300
599 ppm) and still retain the same amount of H_2O in cation defects. However, the question arises
600 whether that amount would be detectable by FTIR, since the amphibole 'shoulder' is more
601 easily distinguishable on an orthopyroxene spectrum than on that of a clinopyroxene due to
602 the latter having absorption bands at higher wavenumbers. We carried out the same spectrum
603 mixing as with orthopyroxene, based on the FPA-FTIR image of a clinopyroxene which did
604 not have adjacent amphibole (in xenolith GN1406 from the Styrian Basin). In the imaged

grain, we distinguished areas with four levels of amphibole content (Fig. 9e), indicated with dark blue ('dry'), light blue, green and red colors and making up approximately 40, 40, 17 and 3 % of the whole mapped area, respectively (Table 3).

Spectrum mixing was applied with the use of the same Perşani Mountains amphibole spectra (Fig. 4c) as with the orthopyroxene. Using the maximum absorbance amphibole spectrum (Fig. 9f), the distinct areas correspond to 0, 2.5, 5 and 10 vol.% amphibole, which yields a total of 1.28 vol.% (1.18 wt.%) after mass balance and dividing with the correction factor. Mixing with the minimum absorbance amphibole (Fig. 9g), the areas represent 10, 20 and 40 vol.% amphibole, equaling to a total corrected proportion of 5.12 vol.% (4.72 wt.%). Using the average amphibole spectrum for mixing (Fig. 9h), the results are 5, 10 and 20 vol.%, for the sub-areas, which corresponds to 2.56 vol.% (2.35 wt.%) amphibole in total. Assuming 2 wt.% water content for the amphibole, the 1.18-4.72 (on average, 2.35) wt.% implies that 236-944 (on average, 470) ppm H_2O is needed to form the lamellae only. Considering 506 ppm for the lamellae-free areas as calculated from the pure clinopyroxene spectrum, the water content of the whole mapped clinopyroxene grain is estimated to be 736-1426 (on average, 964) ppm (Table 3). Similarly to the orthopyroxene, this value is extremely high for upper mantle clinopyroxenes, and water contents in both case are also higher than those obtained in pyroxenes in experiments conducted close to water saturation.

The experimental study of Kovács et al. (2012) found that orthopyroxene and clinopyroxene can have 295 and 980 ppm of H_2O, respectively, at 2.5 GPa and 1000°C, and other experimental works (e.g., Aubaud et al., 2004; Hauri et al., 2006) suggest even higher water contents. The bulk water concentration found in the investigated pyroxenes is higher than it is typical in pyroxenes from the lithospheric mantle from the Carpathian-Pannonian Region (Liptai et al., 2021) and worldwide (i.e., Demouchy and Bolfan-Casanova, 2016; Peslier et al., 2017; Xia et al., 2019). The bulk concentration of water (< 200 ppm wt.) in NAMs from upper mantle xenoliths from the lithospheric mantle may be even less than what was found to be sufficient to stabilize pargasitic amphibole (Kovács et al., 2012; Xia et al., 2019). Even fluids/melts percolating upwards from the asthenosphere may not necessarily increase these water concentration levels in NAMs since water is sequestered from melts/fluids by amphibole precipitation close to the conduits. It also needs to be mentioned, however, that several studies argue that the analyzed water contents of orthopyroxene or even clinopyroxene may not always reliably represent original mantle conditions, as they lose part of their water on their way to the surface or during post eruption cooling (Biró et al., 2017; Tian et al., 2017; Wang et al., 2021).

In summary, the heterogeneous distribution of the amphibole lamellae within the pyroxene grains, evidence of metasomatism by interstitial amphiboles, and the observation that the lamellae appear only in a few grains per sample, we favor the hypothesis that they did not form only by exsolution; instead, an external H_2O source should have been involved. Furthermore, the pre-existence of pyroxene (or spinel) lamellae in the host grain could facilitate amphibole formation, i.e., the amphibole lamellae were likely clinopyroxene lamellae in orthopyroxene before the metasomatism. This explains the source of elements such as Na and Ca which are characteristic components of pargasite but are only trace or minor elements in orthopyroxene. Amphibole lamellae forming at the expense of clinopyroxene with the addition of external water may also explain Fig. 7d, where lamellae in orthopyroxene are observed in optical microscope but only one of them showed amphibole bands on the infrared spectrum. However, if pre-existent clinopyroxene lamellae are lacking, the role of time needed for amphibole formation would be another important factor. Since the diffusion of important elements (Al and Na) in pyroxene structures for amphibole formation is very slow (e.g., Cherniak and Dimanov, 2010) compared to that of H, it takes considerable time. Thus, besides the principally dry nature of the lithospheric mantle beneath the Carpathian-Pannonian region, the geologically short time since the last major tectonic events including the extension (~ 11 Ma) and basin inversion (~ 5 Ma) may have been too short for widespread amphibole exsolution in pyroxenes.

As suggested by hyperspectral images of several grains with neighboring amphibole (Fig. 7e, f), the additional H_2O may come from hydrous melts or fluids percolating along grain boundaries. Both the Styrian Basin and the Perşani Mountains xenoliths represent upper mantle portions infiltrated by subduction-related melts, as supported by their abundant modal amphibole (Aradi et al., 2017; Faccini et al., 2020). However, as evidenced by amphiboles associated with mafic melts (Liptai et al., 2017; Bali et al., 2018; Aradi et al., 2020; Faccini et al., 2020) a supra-subduction environment may not be necessary, nevertheless, the hydrated nature of these marginal parts of the CRP appears to be evident

In the case of grains with no adjacent amphibole or clear sign of melt infiltration, fluid inclusions may provide an explanation for the 'extra' H_2O source. Berkesi et al. (2019) described pargasite inclusions in ortho- and clinopyroxene in xenoliths from Mt. Quincan (Australia), which were associated with fluid inclusions trapped alongside pyroxene lamellae during metasomatism by a fluid with dissolved silicate melt component. The authors proposed that post-extensional cooling led to pargasite formation when the mantle reached the stability field of pargasite. In the samples of our study, fluid inclusions could not be observed in the

673 imaged grain by optical microscope, however, this does not exclude the possibility that they
674 are present on the sub-micron scale as nano-inclusions (see Stenina, 2004 for quartz).
675
676 **6.3. Effect of different tectonic settings in the Carpathian-Pannonian region**
677 Local hydration associated with subduction fluids/melts is easily recognized in the
678 Styrian Basin and Perşani Mountains xenoliths, as evidenced by the abundance of interstitial
679 amphibole and their geochemistry (Aradi et al., 2020; Faccini et al., 2020); although there is
680 no correlation between amphibole modal proportion and whether it is present or not as lamella
681 in the pyroxenes. Generally, all Styrian Basin xenoliths involved in this study have amphibole
682 lamellae in the pyroxenes, yet most of them only have trace amounts of interstitial amphibole
683 (<1 vol.%; Table 1). These samples were interpreted to represent a domain farther from a
684 metasomatic front of a nephelinitic melt that formed amphibole-rich lithologies, such as
685 sample GN1407 (Aradi et al., 2020). In the central localities of the Pannonian Basin (Bakony-
686 Balaton Highland, Nógrád-Gömör), however, amphibole lamellae were found in only one
687 xenolith (Table 1), even though interstitial amphibole is present albeit in lower abundances
688 (Liptai et al., 2017) compared to xenoliths from the marginal regions. Note that while the
689 Bakony-Balaton Highland samples presented in this study contain only traces of amphibole,
690 xenoliths from other quarries of the locality were described to have interstitial amphiboles
691 (Downes et al., 1992; Bali et al., 2002; Szabó et al., 2009; Créon et al., 2017) or rarely even
692 forming amphibole veins (Embey-Isztin, 1976; Bali et al., 2018).
693 In the Nógrád-Gömör, some of the amphiboles have been shown to have subduction-
694 related geochemical characteristics such as low Nb contents, despite being far from any recent
695 subduction zone (Liptai et al., 2017). They were interpreted to represent remnants of a mantle
696 portion affected by subduction-related melts or fluids of presumably Mesozoic age, that
697 predate the formation of the Pannonian Basin (Kovács and Szabó, 2008). Another population
698 of amphiboles was suggested to have formed from, or re-equilibrated with, intraplate mafic
699 melts. Similar genesis was proposed for interstitial and vein amphiboles in several studies
700 focusing on the Bakony-Balaton Highland (Szabó et al., 2009; Bali et al., 2018). These
701 amphiboles are suggested to have formed after the Miocene extension, because the intraplate
702 mafic melts are linked to the same magma production event that resulted in the basaltic
703 volcanism occurring after the cessation of the extension and bringing the xenoliths to the
704 surface (Kovács et al., 2020). Furthermore, the extension and related asthenosphere upwelling
705 resulted in a significant temperature increase which could have caused the breakdown of

amphiboles, as evidenced by melt pockets frequently found in the Bakony-Balaton Highland (Bali et al., 2002; 2007; 2008) and occasionally in the Nógrád-Gömör (Liptai et al., 2017) (Fig. 2c). Since the extension-related decompression was suggested to be responsible for H_2O loss in the NAMs (Patkó et al., 2019), the low H_2O budget of the bulk mantle did not favor amphibole formation, even though it entered the pargasite stability field during the post-extensional cooling. This supports our suggestion that the portions of the upper mantle that were subjected to extension and lithospheric thinning were not able to facilitate subsolidus amphibole formation, hence the general lack of amphibole lamellae and low abundance of interstitial amphibole in the Nógrád-Gömör xenoliths (Table 1).

It is worth noting that in wehrlite xenoliths of the Nógrád-Gömör, which represent products of the most recent metasomatic event (Patkó et al., 2020), 'dry' and 'wet' (low and high H_2O-) clinopyroxene grains were distinguished, even within single samples (Patkó et al., 2019). These may also represent local H_2O enrichment, similar to the pyroxene grains containing amphibole lamellae in the Styrian Basin and the Perşani Mountains, although no connection was found between H_2O content and trace element enrichment which would represent the degree of metasomatism. However, the lack of amphibole lamellae in these 'wet' grains may be due to the fact that the wehrlite-forming metasomatism was still ongoing at the time of xenolith entrainment by the host basalt (Patkó et al., 2020), thus the amount of time to form lamellae in a detectable size may not have been sufficient. Another factor that needs to be taken into account is that the possibility of amphibole lamellae formation does not depend on the availability of H_2O only. The mobility of cations needed to form amphibole, such as Na and Ca is much more limited compared to that of H (e.g., Cherniak and Dimanov, 2010), which might restrict the formation of amphibole lamellae. An exception is, as stated above, if these elements are already present in clinopyroxene lamellae within orthopyroxene, and thus can form amphibole upon the addition of H_2O.

7. Implications

Our study provided insight into the genesis of (pargasitic) amphibole at lithospheric mantle conditions. Amphibole is generally considered a metasomatic product; however, when there is no direct petrographic evidence for metasomatism, the formation may be questionable. The method we applied, using hyperspectral imaging to estimate the volume proportion of amphibole lamellae in pyroxene grains, and using it to quantify the water content for the whole grain, offers a way to prove metasomatic origin. The method involves

740 the determination of a correction factor for different sample thicknesses, which represents the
741 ratio of total polarized vs. unpolarized absorption in the amphibole spectrum in a semi-
742 quantitative way, and thus solving the problem of overestimation of amphibole proportion
743 resulting from using unpolarized light. The amount of amphibole lamellae we observed in the
744 studied Carpathian-Pannonian region xenoliths, along with the water concentrations of the
745 lamella-free pyroxene adds up to water contents unrealistically high for mantle pyroxenes,
746 even in a well-hydrated, supra-subduction environment. Therefore, subsolidus exsolution can
747 be excluded, meaning that the water must come from an external source (i.e., metasomatic
748 melt or fluid).

749 Our results also demonstrate that mobile components, water in particular, can be
750 effectively sequestered from metasomatic fluids by amphibole precipitation in pyroxenes. The
751 consumption of fluids and the precipitation of amphiboles can contribute to explaining the
752 existing rheological contrast between the lithosphere and asthenosphere (Kovács et al., 2021).
753 Consequently, it may represent a key factor in large-scale geodynamic processes, as water
754 sequestration by amphibole leads to the rheological strengthening of the mantle, and thus can
755 contribute to the conversion of the uppermost asthenospheric layer to lithosphere during post-
756 extensional thermal cooling.
757

758 **Acknowledgements**

759

760 We are thankful to Dóra Kesjár for help with the FTIR analyses. This study was
761 financially supported by the MTA FI Lendület Pannon LitH_2Oscope Research Group and the
762 NKFIH K141956 Topo-Transylvania grant. JAPN acknowledges financial support from the
763 Spanish MICINN through the Ramón y Cajal fellowship (RYC2018-024363-I). We are
764 grateful for the thorough and constructive comments of David M. Jenkins and an anonymous
765 reviewer, and the editorial handling by Anne Peslier.
766

767 **References**

768

769 Andrut, M., Brandstätter, F., and Beran, A. (2003) Trace hydrogen zoning in diopside.
770 Mineralogy and Petrology, 78(3), 231-241.

771 Aradi, L.E., Bali, E., Patkó, L., Hidas, K., Kovács, I.J., Zanetti, A., Garrido, C.J., and
772 Szabó, C. (2020) Geochemical evolution of the lithospheric mantle beneath the Styrian Basin
773 (Western Pannonian Basin). Lithos, 378-379, 105831.

774 Aradi, L.E., Hidas, K., Kovács, I.J., Tommasi, A., Klébesz, R., Garrido, C.J., and
775 Szabó, C. (2017) Fluid-enhanced annealing in the subcontinental lithospheric mantle beneath
776 the westernmost margin of the Carpathian-Pannonian extensional basin system. Tectonics,
777 36(12), 2987-3011.
778 Aubaud, C., Hauri, E.H., and Hirschmann, M.M. (2004) Hydrogen partition coefficients
779 between nominally anhydrous minerals and basaltic melts. Geophysical Research Letters,
780 31(20).
781 Bali, E., Falus, G., Szabó, C., Peate, D.W., Hidas, K., Török, K., and Ntaflos, T. (2007)
782 Remnants of boninitic melts in the upper mantle beneath the central Pannonian Basin?
783 Mineralogy and Petrology, 90, 51-72.
784 Bali, E., Hidas, K., Guðfinnsson, G.H., Kovács, Z., Török, K., and Román-Alpiste, M.J.
785 (2018) Zircon and apatite-bearing pyroxene hornblendite mantle xenolith from Hungary,
786 Carpathian-Pannonian region. Lithos, 316, 19-32.
787 Bali, E., Szabó, C., Vaselli, O., and Török, K. (2002) Significance of silicate melt
788 pockets in upper mantle xenoliths from the Bakony-Balaton Highland Volcanic Field,
789 Western Hungary. Lithos, 61, 79-102.
790 Bali, E., Zanetti, A., Szabó, C., Peate, D., and Waight, T. (2008) A micro-scale
791 investigation of melt production and extraction in the upper mantle based on silicate melt
792 pockets in ultramafic xenoliths from the Bakony–Balaton Highland Volcanic Field (Western
793 Hungary). Contributions to Mineralogy and Petrology, 155(2), 165-179.
794 Bell, D.R., Ihinger, P.D., and Rossman, G.R. (1995) Quantitative analysis of trace OH
795 in garnet and pyroxenes. American Mineralogist, 80(5), 465-474.
796 Berkesi, M., Czuppon, G., Szabó, C., Kovács, I., Ferrero, S., Boiron, M.-C., and
797 Peiffert, C. (2019) Pargasite in fluid inclusions of mantle xenoliths from northeast Australia
798 (Mt. Quincan): evidence of interaction with asthenospheric fluid. Chemical Geology, 508,
799 182-196.
800 Biró, T., Kovács, I. J., Karátson, D., Stalder, R., Király, E., Falus, G., Fancsik, T., and
801 Sándorné, J. K. (2017) Evidence for post-depositional diffusional loss of hydrogen in quartz
802 phenocryst fragments within ignimbrites. American Mineralogist, 102(6), 1187-1201.
803 Cherniak D. J. and Dimanov A. (2010) Diffusion in pyroxene, mica and amphibole.
804 Rev. Mineral. Geochem., 72, 641–690.
805 Coltorti, M., Bonadiman, C., Faccini, B., Grégoire, M., O'Reilly, S.Y., and Powell, W.
806 (2007a) Amphiboles from suprasubduction and intraplate lithospheric mantle. Lithos, 99(1),
807 68-84.

Coltorti, M., Bonadiman, C., Faccini, B., Ntaflos, T., and Siena, F. (2007b) Slab melt and intraplate metasomatism in Kapfenstein mantle xenoliths (Styrian Basin, Austria). Lithos, 94(1-4), 66-89.

Créon, L., Delpech, G., Rouchon, V., and Guyot, F. (2017) Slab-derived metasomatism in the Carpathian-Pannonian mantle revealed by investigations of mantle xenoliths from the Bakony-Balaton Highland Volcanic Field. Lithos, 286, 534-552.

Dawson, J., and Smith, J. (1982) Upper-mantle amphiboles: a review. Mineralogical Magazine, 45(337), 35-46.

Day, M.C., Hawthorne, F.C., Susta, U., Della Ventura, G., and Harlow, G.E. (2018) Short-Range Order-Disorder in Gem Richterite and Pargasite from Afghanistan: Crystal-Structure Refinement and Infrared Spectroscopy. The Canadian Mineralogist, 56(6), 939-950.

Della Ventura, G., Hawthorne, F.C., Robert, J.-L., Delbove, F., Welch, M.F., and Raudsepp, M. (1999) Short-range order of cations in synthetic amphiboles along the richterite-pargasite join. European Journal of Mineralogy, 11(1), 79-94.

Della Ventura, G., Hawthorne, F.C., Robert, J.-L., and Iezzi, G. (2003) Synthesis and infrared spectroscopy of amphiboles along the tremolite-pargasite join. European Journal of Mineralogy, 15(2), 341-347.

Della Ventura, G., Oberti, R., Hawthorne, F.C., and Bellatreccia, F. (2007) FTIR spectroscopy of Ti-rich pargasites from Lherz and the detection of O2− at the anionic O3 site in amphiboles. American Mineralogist, 92(10), 1645-1651.

Della Ventura, G., Robert, J.-L., Sergent, J., Hawthorne, F.C., and Delbove, F. (2001) Constraints on F vs. OH incorporation in synthetic [6] Al-bearing monoclinic amphiboles. European Journal of Mineralogy, 13(5), 841-847.

Demers-Roberge, A., Jollands, M.C., Tollan, P., and Müntener, O. (2021) H diffusion in orthopyroxene and the retention of mantle water signatures. Geochimica et Cosmochimica Acta, 305, 263-281.

Demouchy, S., and Bolfan-Casanova, N. (2016) Distribution and transport of hydrogen in the lithospheric mantle: A review. Lithos, 240, 402-425.

Downes, H., Embey-Isztin, A., and Thirlwall, M.F. (1992) Petrology and geochemistry of spinel peridotite xenoliths from the western Pannonian Basin (Hungary): evidence for an association between enrichment and texture in the upper mantle. Contributions to Mineralogy and Petrology, 109(3), 340-354.

Embey-Isztin, A. (1976) Amphibole/lherzolite composite xenoliths from Szigliget, north of Lake Balaton, Hungary. Earth and Planetary Science Letters, 31, 297-304.

Ernst, W., and Wai, C. (1970) Mössbauer, infrared, X-ray and optical study of cation ordering and dehydrogenation in natural and heat-treated sodic amphiboles. American Mineralogist: Journal of Earth and Planetary Materials, 55(7-8), 1226-1258.

Faccini, B., Rizzo, A.L., Bonadiman, C., Ntaflos, T., Seghedi, I., Grégoire, M., Ferretti, G., and Coltorti, M. (2020) Subduction-related melt refertilisation and alkaline metasomatism in the Eastern Transylvanian Basin lithospheric mantle: Evidence from mineral chemistry and noble gases in fluid inclusions. Lithos, 364, 105516.

Facer, J., Downes, H., and Beard, A. (2009) In situ Serpentinization and Hydrous Fluid Metasomatism in Spinel Dunite Xenoliths from the Bearpaw Mountains, Montana, USA. Journal of Petrology, 50(8), 1443-1475.

Falus, G., Tommasi, A., Ingrin, J., and Szabó, C. (2008) Deformation and seismic anisotropy of the lithospheric mantle in the southeastern Carpathians inferred from the study of mantle xenoliths. Earth and Planetary Science Letters, 272(1–2), 50-64.

Fialips-Guédon, C.-I., Robert, J.-L., and Delbove, F. (2000) Experimental study of Cr incorporation in pargasite. American Mineralogist, 85(5-6), 687-693.

Gose, J., Schmädicke, E., and Stalder, R. (2011) Water in mantle orthopyroxene – no visible change in defect water during serpentinization. European Journal of Mineralogy, 23(4), 529-536.

Green, D.H. (1973) Experimental melting studies on a model upper mantle composition at high pressure under water-saturated and water-undersaturated conditions. Earth and Planetary Science Letters, 19(1), 37-53.

Green, D.H. (2015) Experimental petrology of peridotites, including effects of water and carbon on melting in the Earth's upper mantle. Physics and Chemistry of Minerals, 42(2), 95-122.

Green, D.H., Hibberson, W.O., Kovács, I., and Rosenthal, A. (2010) Water and its influence on the lithosphere-asthenosphere boundary. Nature, 467(7314), 448-451.

Hauri, E.H., Gaetani, G.A., and Green, T.H. (2006) Partitioning of water during melting of the Earth's upper mantle at H 2 O-undersaturated conditions. Earth and Planetary Science Letters, 248(3), 715-734.

Hawthorne, F.C., Oberti, R., Harlow, G.E., Maresch, W.V., Martin, R.F., Schumacher, J.C., and Welch, M.D. (2012) Nomenclature of the amphibole supergroup. American Mineralogist, 97(11-12), 2031-2048.

Heaveysege, D., Abdu, Y.A., and Hawthorne, F.C. (2015) Long-range and short-range order in gem pargasite from Myanmar: Crystal-structure refinement and infrared spectroscopy. The Canadian Mineralogist, 53(3), 497-510.

Hidas, K., Guzmics, T., Szabó, C., Kovács, I., Bodnar, R.J., Zajacz, Z., Nédli, Z., Vaccari, L., and Perucchi, A. (2010) Coexisting silicate melt inclusions and H2O-bearing, CO2-rich fluid inclusions in mantle peridotite xenoliths from the Carpathian-Pannonian region (central Hungary). Chemical Geology, 274(1-2), 1-18.

Horváth, F. (1993) Towards a mechanical model for the formation of the Pannonian basin. Tectonophysics, 226(1-4), 333-357.

Horváth, F., Musitz, B., Balázs, A., Végh, A., Uhrin, A., Nádor, A., Koroknai, B., Pap, N., Tóth, T., and Wórum, G. (2015) Evolution of the Pannonian basin and its geothermal resources. Geothermics, 53, 328-352.

Ingrin, J., Latrous, K., Doukhan, J.-C., and Doukhan, N. (1989) Water in diopside: an electron microscopy and infrared spectroscopy study. European Journal of Mineralogy, 327-342.

Isaacs, A.M., Brown, P.E., Valley, J.W., Essene, E.J., and Peacor, D.R. (1981) An analytical electron microscopic study of a pyroxene-amphibole intergrowth. Contributions to Mineralogy and Petrology, 77(2), 115-120.

Ishida, K., Jenkins, D.M., and Hawthorne, F.C. (2008) Mid-IR bands of synthetic calcic amphiboles of tremolite-pargasite series and of natural calcic amphiboles. American Mineralogist, 93(7), 1112-1118.

Jenkins, D.M., Bozhilov, K.N., and Ishida, K. (2003) Infrared and TEM characterization of amphiboles synthesized near the tremolite-pargasite join in the ternary system tremolite-pargasite-cummingtonite. American Mineralogist, 88(7), 1104-1114.

Jollands, M.C., Padrón-Navarta, J.A., Hermann, J., and O'Neill, H.S.C. (2016) Hydrogen diffusion in Ti-doped forsterite and the preservation of metastable point defects. American Mineralogist, 101(7), 1571-1583.

Kang, P., Lamb, W.M., and Drury, M. (2017) Using mineral equilibria to estimate H2O activities in peridotites from the Western Gneiss Region of Norway. American Mineralogist, 102(5), 1021-1036.

Kovács, I., Hermann, J., O'Neill, H. S. C., Gerald, J. F., Sambridge, M., and Horváth, G. (2008) Quantitative absorbance spectroscopy with unpolarized light: Part II. Experimental evaluation and development of a protocol for quantitative analysis of mineral IR spectra. American Mineralogist, 93(5-6), 765-778.

Kovács, I., Green, D.H., Rosenthal, A., Hermann, J., O'Neill, H.S.C., Hibberson, W.O., and Udvardi, B. (2012) An experimental study of water in nominally anhydrous minerals in the upper mantle near the water-saturated solidus. Journal of Petrology, 53, 2067-2093.

Kovács, I., Lenkey, L., Green, D.H., Fancsik, T., Falus, G., Kiss, J., Orosz, L., Angyal, J., and Vikor, Z. (2017) The role of pargasitic amphibole in the formation of major geophysical discontinuities in the shallow upper mantle. Acta Geodaetica et Geophysica, 52(2), 183-204.

Kovács, I., Patkó, L., Liptai, N., Lange, T.P., Taracsák, Z., Cloetingh, S.A.P.L., Török, K., Király, E., Karátson, D., Biró, T., Kiss, J., Pálos, Z., Aradi, L.E., Falus, G., Hidas, K., Berkesi, M., Koptev, A., Novák, A., Wesztergom, V., and Szabó, C. (2020) The role of water and compression in the genesis of alkaline basalts: Inferences from the Carpathian-Pannonian region. Lithos, 354, 105323-105323.

Kovács, I., and Szabó, C. (2008) Middle Miocene volcanism in the vicinity of the Middle Hungarian zone: Evidence for an inherited enriched mantle source. Journal of Geodynamics, 45(1), 1-17.

Kovács, I., Zajacz, Z., and Szabó, C. (2004) Type-II xenoliths and related metasomatism from the Nógrád-Gömör Volcanic Field, Carpathian-Pannonian region (northern Hungary–southern Slovakia). Tectonophysics, 393(1-4), 139-161.

Kovács, I.J., Liptai, N., Koptev, A., Cloetingh, S.A.P.L., Lange, T.P., Mațenco, L., Szakács, A., Radulian, M., Berkesi, M., Patkó, L., Molnár, G., Novák, A., Wesztergom, V., Szabó, C., and Fancsik, T. (2021) The 'pargasosphere' hypothesis: Looking at global plate tectonics from a new perspective. Global and Planetary Change, 103547.

Kurat, G., Palme, H., Spettel, B., Baddenhausen, H., Hofmeister, H., Palme, C., and Wanke, H. (1980) Geochemistry of Ultramafic Xenoliths from Kapfenstein, Austria - Evidence for a Variety of Upper Mantle Processes. Geochimica Et Cosmochimica Acta, 44(1), 45-&.

Kushiro, I. (1970) Stability of amphibole and phlogopite in the upper mantle. Carnegie Institute of Washington Yearbook, 68, 245-247.

Libowitzky, E., and Rossman, G. R. (1996) Principles of quantitative absorbance measurements in anisotropic crystals. Physics and Chemistry of Minerals, 23(6), 319-327.

Libowitzky, E., and Rossman, G. R. (1997) An IR absorption calibration for water in minerals. American Mineralogist, 82, 1111-1115.

Liptai, N., Hidas, K., Tommasi, A., Patkó, L., Kovács, I.J., Griffin, W.L., O'Reilly, S.Y., Pearson, N.J., and Szabó, C. (2019) Lateral and Vertical Heterogeneity in the

Lithospheric Mantle at the Northern Margin of the Pannonian Basin Reconstructed From Peridotite Xenolith Microstructures. Journal of Geophysical Research: Solid Earth, 124(7), 6315-6336.

Liptai, N., Lange, T.P., Patkó, L., Pintér, Z., Berkesi, M., Aradi, L.E., Szabó, C., and Kovács, I.J. (2021) Effect of water on the rheology of the lithospheric mantle in young extensional basin systems as shown by xenoliths from the Carpathian-Pannonian region. Global and Planetary Change, 196, 103364.

Liptai, N., Patkó, L., Kovács, I.J., Hidas, K., Pintér, Z., Jeffries, T., Zajacz, Z., O'Reilly, S.Y., Griffin, W.L., Pearson, N.J., and Szabó, C. (2017) Multiple metasomatism beneath the Nógrád–Gömör Volcanic Field (Northern Pannonian Basin) revealed by upper mantle peridotite xenoliths. Journal of Petrology, 58(6), 1107-1144.

Madejová, J., Gates, W.P., and Petit, S. (2017) Chapter 5 - IR Spectra of Clay Minerals. In W.P. Gates, J.T. Kloprogge, J. Madejová, and F. Bergaya, Eds. Developments in Clay Science, 8, p. 107-149. Elsevier.

Mandler, B.E., and Grove, T.L. (2016) Controls on the stability and composition of amphibole in the Earth's mantle. Contributions to Mineralogy and Petrology, 171(8), 1-20.

Moody, J.B. (1976) Serpentinization: a review. Lithos, 9(2), 125-138.

Niida, K., and Green, D.H. (1999) Stability and chemical composition of pargasitic amphibole in MORB pyrolite under upper mantle conditions. Contributions to Mineralogy and Petrology, 135(1), 18-40.

Noack, Y., Colin, F., Nahon, D., Delvigne, J., and Michaux, L. (1993) Secondary-mineral formation during natural weathering of pyroxene; review and thermodynamic approach. American Journal of Science, 293(2), 111-134.

O'Reilly, S.Y., and Griffin, W. (2013) Mantle metasomatism. In D.E. Harlov, and H. Austrheim, Eds. Metasomatism and the Chemical Transformation of Rock, p. 471-533. Springer.

Padrón-Navarta, J.A., Hermann, J., Garrido, C.J., Sánchez-Vizcaíno, V.L., and Gómez-Pugnaire, M.T. (2010) An experimental investigation of antigorite dehydration in natural silica-enriched serpentinite. Contributions to Mineralogy and Petrology, 159(1), 25.

Patkó, L., Liptai, N., Aradi, L.E., Klébesz, R., Sendula, E., Bodnar, R.J., Kovács, I.J., Hidas, K., Cesare, B., Novák, A., Trásy, B., and Szabó, C. (2020) Metasomatism-induced wehrlite formation in the upper mantle beneath the Nógrád-Gömör Volcanic Field (Northern Pannonian Basin): Evidence from xenoliths. Geoscience Frontiers, in press.

Patkó, L., Liptai, N., Kovács, I.J., Aradi, L.E., Xia, Q.-K., Ingrin, J., Mihály, J., O'Reilly, S.Y., Griffin, W.L., Wesztergom, V., and Szabó, C. (2019) Extremely low structural hydroxyl contents in upper mantle xenoliths from the Nógrád-Gömör Volcanic Field (northern Pannonian Basin): Geodynamic implications and the role of post-eruptive re-equilibration. Chemical Geology, 507, 23-41.

Peslier, A. H., Schönbächler, M., Busemann, H., and Karato, S-I. (2017), Water in the Earth's interior: Distribution and origin. Space Science Reviews, 212(1), 743-811.Phillips, M.W., Draheim, J.E., Popp, R.K., Clowe, C.A., and Pinkerton, A.A. (1989) Effects of oxidation-dehydrogenation in tschermakitic hornblende. American Mineralogist, 74(7-8), 764-773.

Popp, R.K., Virgo, D., and Phillips, M.W. (1995) H deficiency in kaersutitic amphiboles: Experimental verification. American Mineralogist, 80(11-12), 1347-1350.

Qiu, Y., Jiang, H., Kovács, I., Xia, Q. K., and Yang, X. (2018) Quantitative analysis of H-species in anisotropic minerals by unpolarized infrared spectroscopy: An experimental evaluation. American Mineralogist: Journal of Earth and Planetary Materials, 103(11), 1761-1769.

Rauch, M., and Keppler, H. (2002) Water solubility in orthopyroxene. Contributions to Mineralogy and Petrology, 143(5), 525-536.

Robert, J.-L., Della Ventura, G., Welch, M.D., and Hawthorne, F.C. (2000) The OH-F substitution in synthetic pargasite at 1.5 kbar, 850 C. American Mineralogist, 85(7-8), 926-931.

Robert, J.-L., Ventura, G.D., and Hawthorne, F.C. (1999) Near-infrared study of short-range disorder of OH and F in monoclinic amphiboles. American Mineralogist, 84(1-2), 86-91.

Sambridge, M., Gerald, J. F., Kovács, I., O'Neill, H. S. C., and Hermann, J. (2008) Quantitative absorbance spectroscopy with unpolarized light: Part I. Physical and mathematical development. American Mineralogist, 93(5-6), 751-764.

Skogby, H., Bell, D.R., and Rossman, G.R. (1990) Hydroxide in pyroxene; variations in the natural environment. American Mineralogist, 75(7-8), 764-774.

Skogby, H., and Rossman, G.R. (1989) OH-in pyroxene; an experimental study of incorporation mechanisms and stability. American Mineralogist, 74(9-10), 1059-1069.

Skogby, H., and Rossman, G. R. (1991) The intensity of amphibole OH bands in the infrared absorption spectrum. Physics and Chemistry of Minerals, 18(1), 64-68.

Smith, P.P.K. (1977) An electron microscopic study of amphibole lamellae in augite. Contributions to Mineralogy and Petrology, 59(3), 317-322.

Song, S., Zhang, L., Chen, J., Liou, J.G., and Niu, Y. (2005) Sodic amphibole exsolutions in garnet from garnet-peridotite, North Qaidam UHPM belt, NW China: Implications for ultradeep-origin and hydroxyl defects in mantle garnets. American Mineralogist, 90(5-6), 814-820.

Stenina, N.G. (2004) Water-related defects in quartz. Bulletin of Geosciences, 79, 251–268.

Sundvall, R., and Stalder, R. (2011) Water in upper mantle pyroxene megacrysts and xenocrysts: A survey study. American Mineralogist, 96(8-9), 1215-1227.

Szabó, C., Hidas, K., Bali, E., Zajacz, Z., Kovács, I., Yang, K., Guzmics, T., and Török, K. (2009) Melt-wall rock interaction in the mantle shown by silicate melt inclusions in peridotite xenoliths from the central Pannonian Basin (western Hungary). Island Arc, 18(2), 375-400.

Szabó, C., and Taylor, L.A. (1994) Mantle petrology and geochemistry beneath the Nógrád-Gömör Volcanic Field, Carpathian-Pannonian Region. International Geology Review, 36(4), 328-358.

Tian, Z.-Z., Liu, J., Xia, Q.-K., Ingrin, J., Hao, Y.-T., and Christophe, D. (2017) Water concentration profiles in natural mantle orthopyroxenes: A geochronometer for long annealing of xenoliths within magma. Geology, 45(1), 87-90.

Tollan, P., and Hermann, J. (2019) Arc magmas oxidized by water dissociation and hydrogen incorporation in orthopyroxene. Nature Geoscience, 12(8), 667-671.

Tommasi, A., Langone, A., Padrón-Navarta, J.A., Zanetti, A., and Vauchez, A. (2017) Hydrous melts weaken the mantle, crystallization of pargasite and phlogopite does not: Insights from a petrostructural study of the Finero peridotites, southern Alps. Earth and Planetary Science Letters, 477, 59-72.

Ulmer, P., and Trommsdorff, V. (1995) Serpentine Stability to Mantle Depths and Subduction-Related Magmatism. Science, 268(5212), 858-861.

Vaselli, O., Downes, H., Thirlwall, M.F., Dobosi, G., Coradossi, N., Seghedi, I., Szakács, A., and Vannucci, R. (1995) Ultramafic xenoliths in Plio-Pleistocene alkali basalts from the eastern Transylvanian Basin: depleted mantle enriched by vein metasomatism. Journal of Petrology, 36(1), 23-53.

Veblen, D.R., and Buseck, P.R. (1981) Hydrous pyriboles and sheet silicates in pyroxenes and uralites: intergrowth microstructures and reaction mechanisms, American Mineralogist, 66, 1107-1134.

Wallace, M., and Green, D. (1991) The effect of bulk rock composition on the stability of amphibole in the upper mantle: implications for solidus positions and mantle metasomatism. Mineralogy and Petrology, 44(1), 1-19.

Wang, Y.-F., Qin, J.-Y., Soustelle, V., Zhang, J.-F., and Xu, H.-J. (2021) Pyroxene does not always preserve its source hydrogen concentration: Clues from some peridotite xenoliths. Geochimica et Cosmochimica Acta, 292, 382-408.

Withers, A. C. (2013) On the use of unpolarized infrared spectroscopy for quantitative analysis of absorbing species in birefringent crystals. American Mineralogist, 98(4), 689-697.

Xia, Q.-K., Liu, J., Liu, S.-C., Kovács, I., Feng, M., and Dang, L. (2013) High water content in Mesozoic primitive basalts of the North China Craton and implications on the destruction of cratonic mantle lithosphere. Earth and Planetary Science Letters, 361, 85-97.

Xia, Q. K., Liu, J., Kovács, I., Hao, Y. T., Li, P., Yang, X. Z., Chen, H., and Sheng, Y. M. (2019) Water in the upper mantle and deep crust of eastern China: concentration, distribution and implications. National Science Review, 6(1), 125-144.

1058

Sample	Thickness (μm)	Interstitial amphibole?	n. of grains analyzed	Analyses	Band position of hydrous lamella (cm^{-1})	Amphibole lamella?	Other hydrous phases?
Styrian Basin							
BEI1401	180	yes	1	FTIR	3710	yes	no
GN1401	385	yes	3	FTIR	3695, 3712	yes	yes
GN1406	325	yes (<1%)	1	FTIR+FPA	3680, 3712	yes	no
GN1407	50-80	yes	8	FTIR single spectra only	3683, 3710	-	-
GN1411	235	yes (<1%)	4	FTIR	3680-3685, 3710	yes	no
GN1412	425	yes (<1%)	2	FTIR	3695	no	yes
PST1401	460	yes (<1%)	3	FTIR+FPA	3680	yes	no
PST1403	480	yes (<1%)	1	FTIR	3680	yes	no
TOB1401	385	yes (<1%)	1	FTIR+FPA	3678	yes	no
TOB1403	235	yes	2	FTIR	3708	yes	no
Bakony-Balaton Highland							
FT0101	760	no	3	FTIR+FPA	-	no	no
FT0801	245	no	3	FTIR	-	no	no
FT042	565	no	6	FTIR+FPA	3695	no	yes
FT07	360	yes (<1%)	3	FTIR+FPA	3695	no	yes
FTP5	720	yes (<1%)	-	FTIR	-	-	-
Nógrád-Gömör							
NMS1304	95	yes	-	FTIR single spectra only	-	-	-
NMS1308	275	yes	2	FTIR	-	no	no
NMS1310	280	no	3	FTIR+FPA	3685-3710	yes	no
NJS1306	185	no	3	FTIR	-	no	no
NJS1307	225	no	3	FTIR+FPA	-	no	no
NFL1305	335	no	4	FTIR+FPA	3624, 3696	no	yes
NFL1329	155	yes	3	FTIR	-	no	no
NTB0307	250	no	3	FTIR	3626, 3694	no	yes
NTB1116	300	no	3	FTIR	-	no	no
NTB1124	310	no	3	FTIR	-	no	no
NFK0301	260	no	2	FTIR+FPA	3678	no	yes
NFR1109	255	no	2	FTIR+FPA	3686	no	yes
NMC1336A	220	no	3	FTIR	-	no	no
NBN0302A	125	no	3	FTIR+FPA	-	no	no
NBN0311	335	no	4	FTIR	-	no	no
NBN0321	180	no	2	FTIR	-	no	no
Perşani Mountains							
PGR-X1-0306	355	yes	3	FTIR+FPA	3680, 3697, 3710	yes	yes
PGR-X1-0347	315	yes	2	FTIR+FPA	3680, 3710	yes	no
PGR-X2-0396	290	yes	10	FTIR single spectra only	3656, 3680, 3710	yes	no
PGR-14182	30-80	yes	7	FTIR single spectra only	3654, 3686, 3710	yes	no

1059

1060 Table 1. Summary of amphibole content, analyses and hydrous phases found in pyroxene
1061 grains in the studied xenoliths.

1062

	Normalization		
	1 μm	*10 μm*	*60 μm*
Total integrated polarized absorbance	2.3	23	139
Average total integrated unpolarized absorbance	0.76	6.9	28
Max. total integrated unpolarized absorbance	1.04	9.4	37
Min. total integrated unpolarized absorbance	0.17	1.7	10
Correction factor (average)	**1.01**	**1.12**	**1.68**
Min. correction factor	0.75	0.82	1.26
Max. correction factor	4.6	4.6	4.6

1063

1064 Table 2. Calculation of the average, minimum and maximum correction factor to quantify the
1065 difference in the total polarized vs. unpolarized absorbance for different sample thicknesses.

1066

	Area proportions (%)	Amphibole proportion (vol.%) if mixed with:		
		max. absorbance amp. spectrum	min. absorbance amp. spectrum	averaged amp. spectrum
Orthopyroxene (166 ppm H_2O)				
*dark blue ('dry')	75	0	0	0
*light blue	22	5	15	10
*green	3	10	35	20
Total amphibole vol.% (wt.%)		1.40 (1.37)	4.35 (4.25)	2.80 (2.73)
Corrected total amphibole vol.% (wt.%)		0.83 (0.81)	2.59 (2.53)	1.67 (1.63)
Water needed for amphibole only (ppm)		*162*	*506*	*326*
Water content of the whole grain (ppm)		***327***	***668***	***489***
Clinopyroxene (506 ppm H_2O)				
*dark blue ('dry')	40	0	0	0
*light blue	40	2.5	10	5
*green	17	5	20	10
*red	3	10	40	20
Total amphibole vol.% (wt.%)		2.15 (1.98)	8.60 (7.95)	4.30 (3.96)
Corrected total amphibole vol.% (wt.%)		1.28 (1.18)	5.12 (4.72)	2.56 (2.35)
Water needed for amphibole only (ppm)		*236*	*944*	*470*
Water content of the whole grain (ppm)		***736***	***1426***	***964***

1067

1068 Table 3. Calculations of assumed bulk water contents of orthopyroxene and
1069 clinopyroxene grains imaged with FPA-FTIR (Fig. 9), using spectrum mixing with amphibole
1070 (maximum, minimum and averaged spectra from Fig. 4c). Colors marked with asterisk
1071 represent different proportions of amphibole lamella, as seen on the hyperspectral images
1072 (Fig. 9).

This is the peer-reviewed, final accepted version for American Mineralogist, published by the Mineralogical Society of America.
The published version is subject to change. Cite as Authors (Year) Title. American Mineralogist, in press.
DOI: https://doi.org/10.2138/am-2022-8662. http://www.minsocam.org/

Figure 1

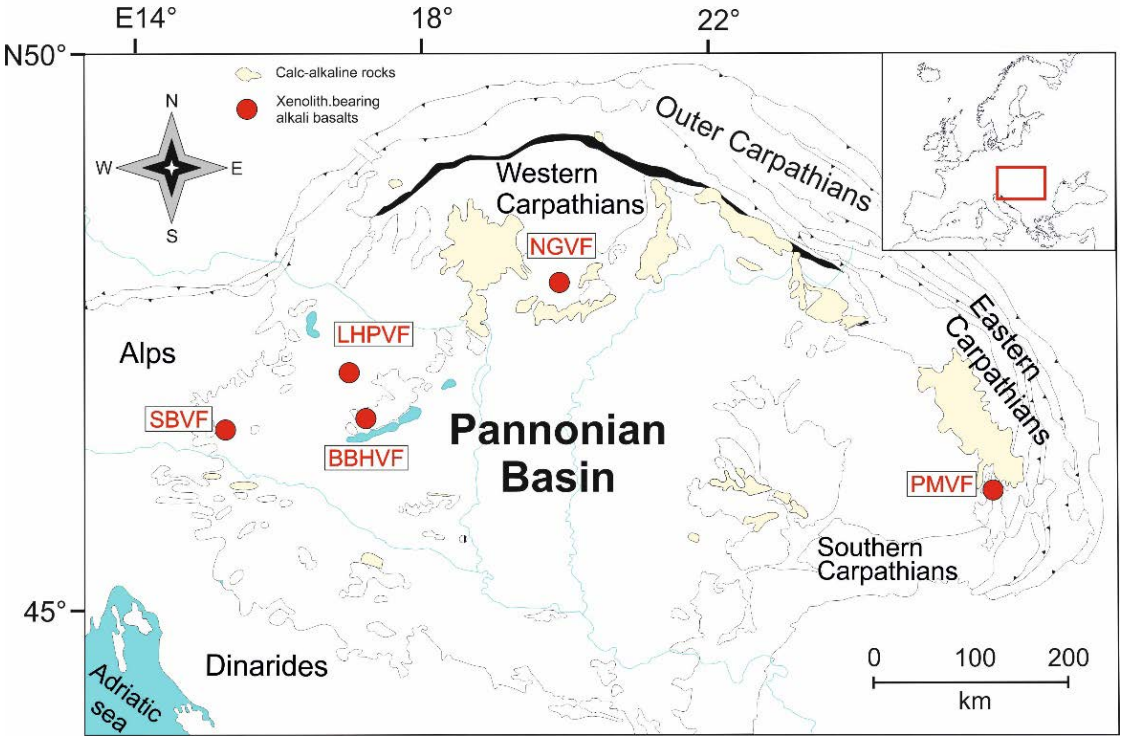

Figure 1. Location of the xenolith-hosting alkali basalt localities within the Carpathian-Pannonian region. Abbreviations: SBVF – Styrian Basin Volcanic Field, LHPVF – Little Hungarian Plain Volcanic Field, BBHVF – Bakony-Balaton Highland Volcanic Field, NGVF – Nógrád-Gömör Volcanic Field, PMVF - Perşani Mountains Volcanic Field.

Figure 2

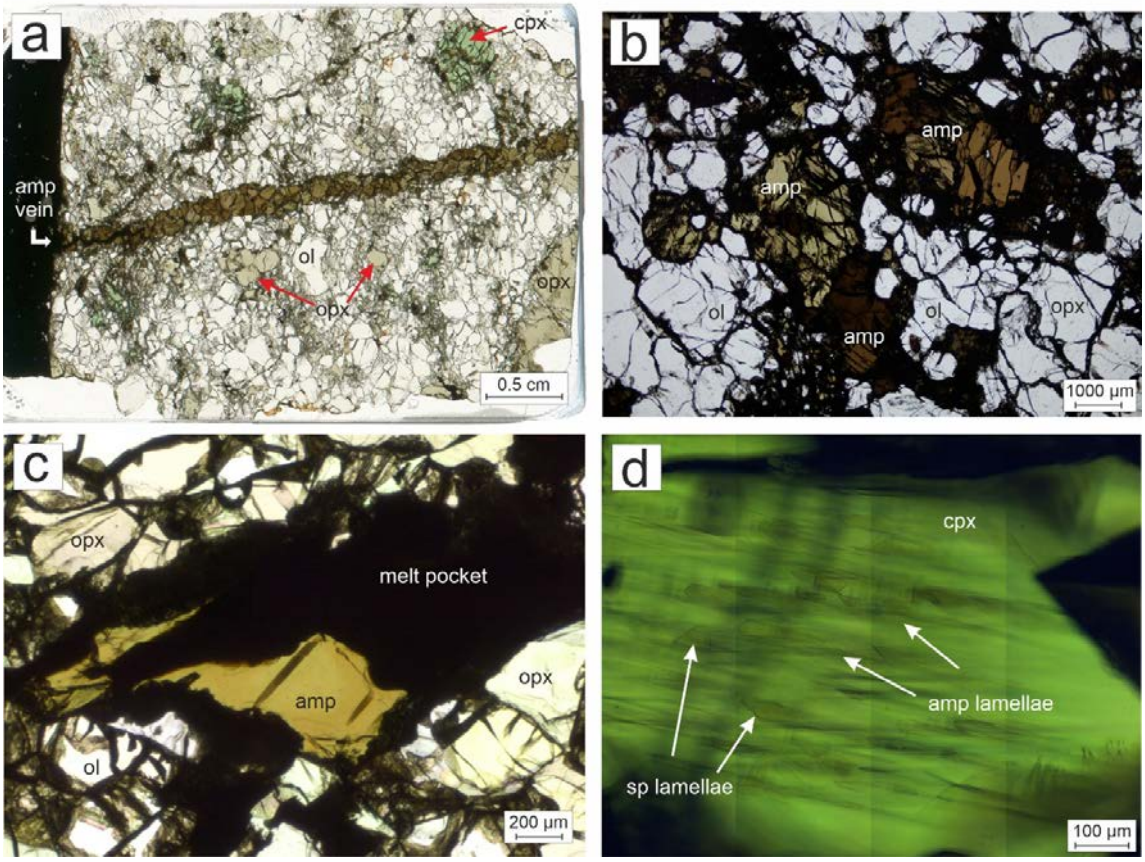

Figure 2. Appearances of amphibole (amp) in xenoliths from the Carpathian-Pannonian region. (a) Amphibolite vein crosscutting a lherzolite from the Perşani Mountains (PGR-X2-0396); scanned thin section image. (b) Interstitial amphibole grains in a Styrian Basin xenolith (BEI1401); transmitted light, 1N. (c) Interstitial amphibole and neighboring melt pocket in a Nógrád-Gömör xenolith (NMS1304); transmitted light, 1N. (d) Amphibole and spinel lamellae in a clinopyroxene (cpx) grain in a Styrian Basin xenolith (GN1406); transmitted light, 1N.

This is the peer-reviewed, final accepted version for American Mineralogist, published by the Mineralogical Society of America.
The published version is subject to change. Cite as Authors (Year) Title. American Mineralogist, in press.
DOI: https://doi.org/10.2138/am-2022-8662. http://www.minsocam.org/

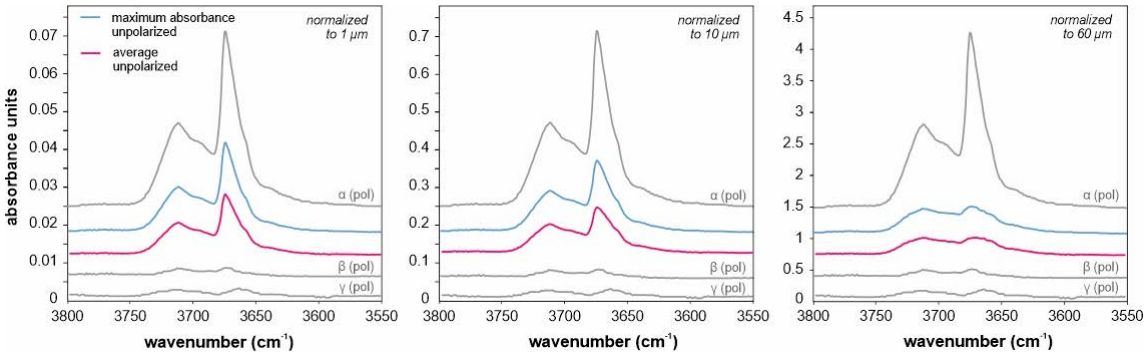

Figure 3. Polarized (pol) sodium cummingtonite spectra taken from Skogby and Rossman (1991), with modelled average and maximum absorbance unpolarized spectra for different sample thicknesses. Minimum unpolarized absorbance is considered close to 0. Correction factors were calculated based on the difference between total polarized and unpolarized absorbances (see text for details).

This is the peer-reviewed, final accepted version for American Mineralogist, published by the Mineralogical Society of America.
The published version is subject to change. Cite as Authors (Year) Title. American Mineralogist, in press.
DOI: https://doi.org/10.2138/am-2022-8662. http://www.minsocam.org/

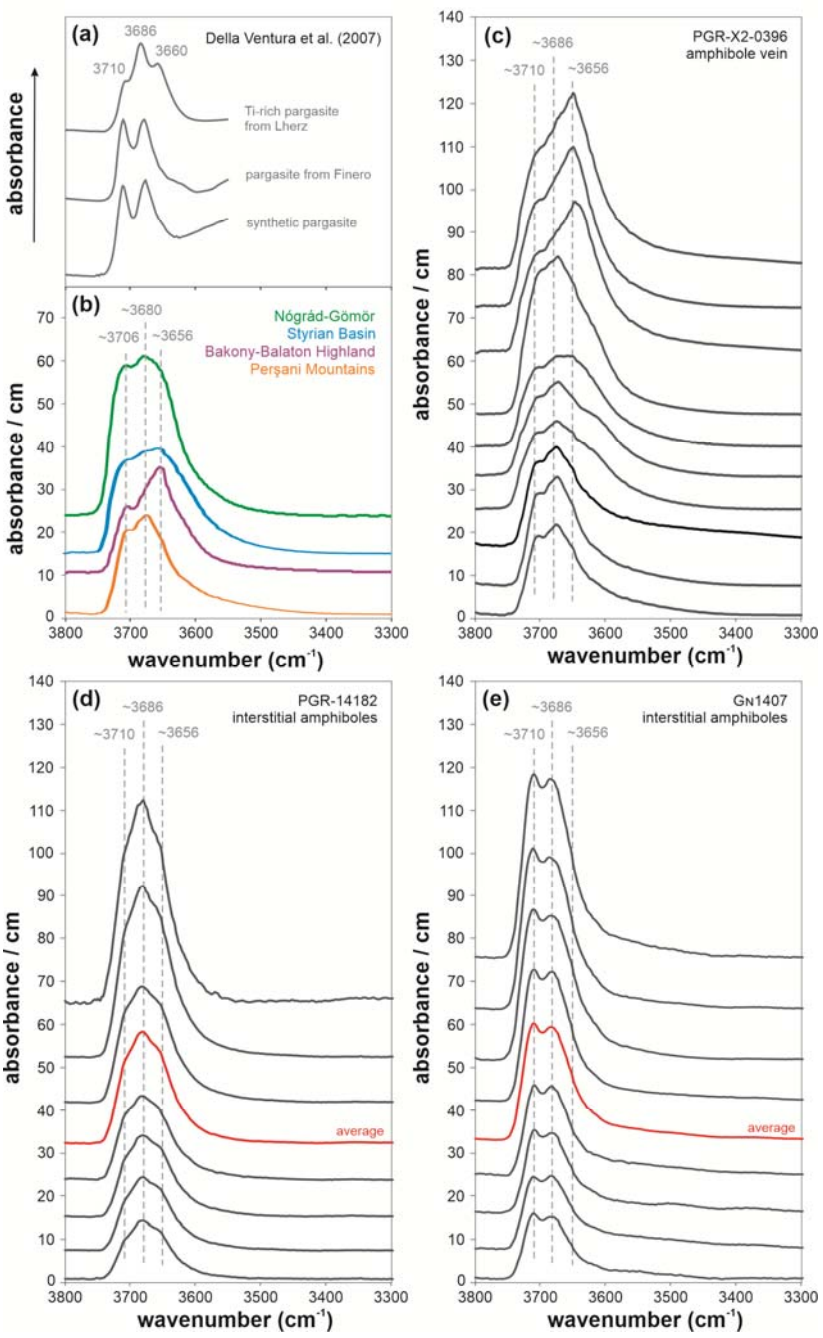

Figure 4. (a) FTIR spectra of natural and synthetic pargasite from the study of Della Ventura et al. (2007). (b) Examples of interstitial amphibole FTIR spectra from localities of the Carpathian-Pannonian region. (c) FTIR spectra of amphibole grains from the amphibole vein in xenolith PGR-X2-0396 (d-e) FTIR spectra of separated amphibole grains, and their average in red, from a Perşani Mountains (PGR-14182) and a Styrian Basin (GN1407) xenolith, respectively. All spectra were obtained with unpolarized light, on single unoriented crystals.

This is the peer-reviewed, final accepted version for American Mineralogist, published by the Mineralogical Society of America.
The published version is subject to change. Cite as Authors (Year) Title. American Mineralogist, in press.
DOI: https://doi.org/10.2138/am-2022-8662. http://www.minsocam.org/

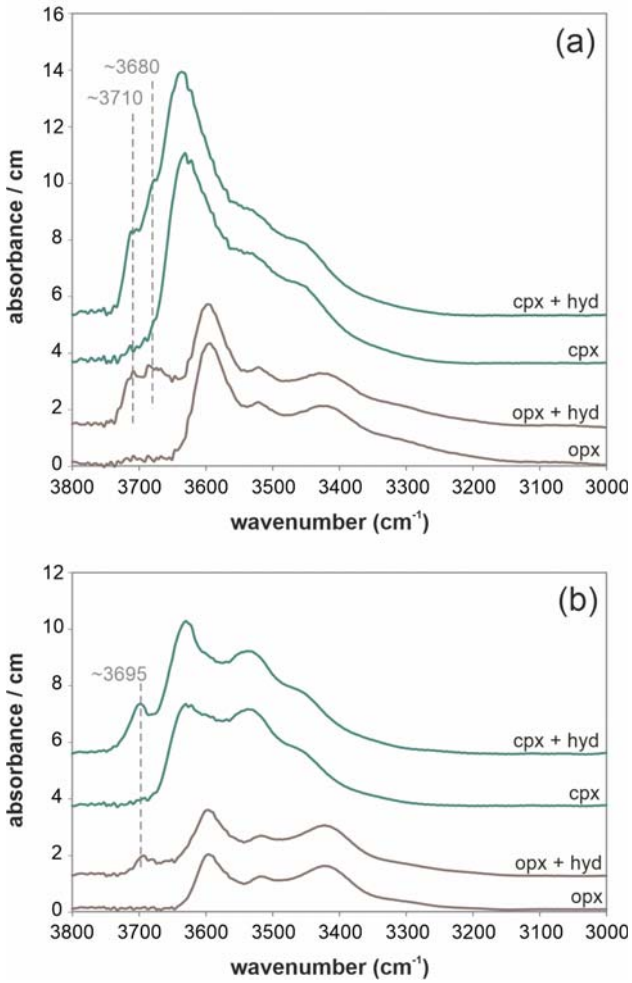

Figure 5. Unpolarized single FTIR spectra of orthopyroxene (opx) and clinopyroxene (cpx) with indication of hydrous phases (hyd) at wavenumbers of ~3710-3680 (a) and ~3695 (b) cm^{-1}. Corresponding spectra free of hydrous phases from the same grains are shown for comparison.

This is the peer-reviewed, final accepted version for American Mineralogist, published by the Mineralogical Society of America.
The published version is subject to change. Cite as Authors (Year) Title. American Mineralogist, in press.
DOI: https://doi.org/10.2138/am-2022-8662. http://www.minsocam.org/

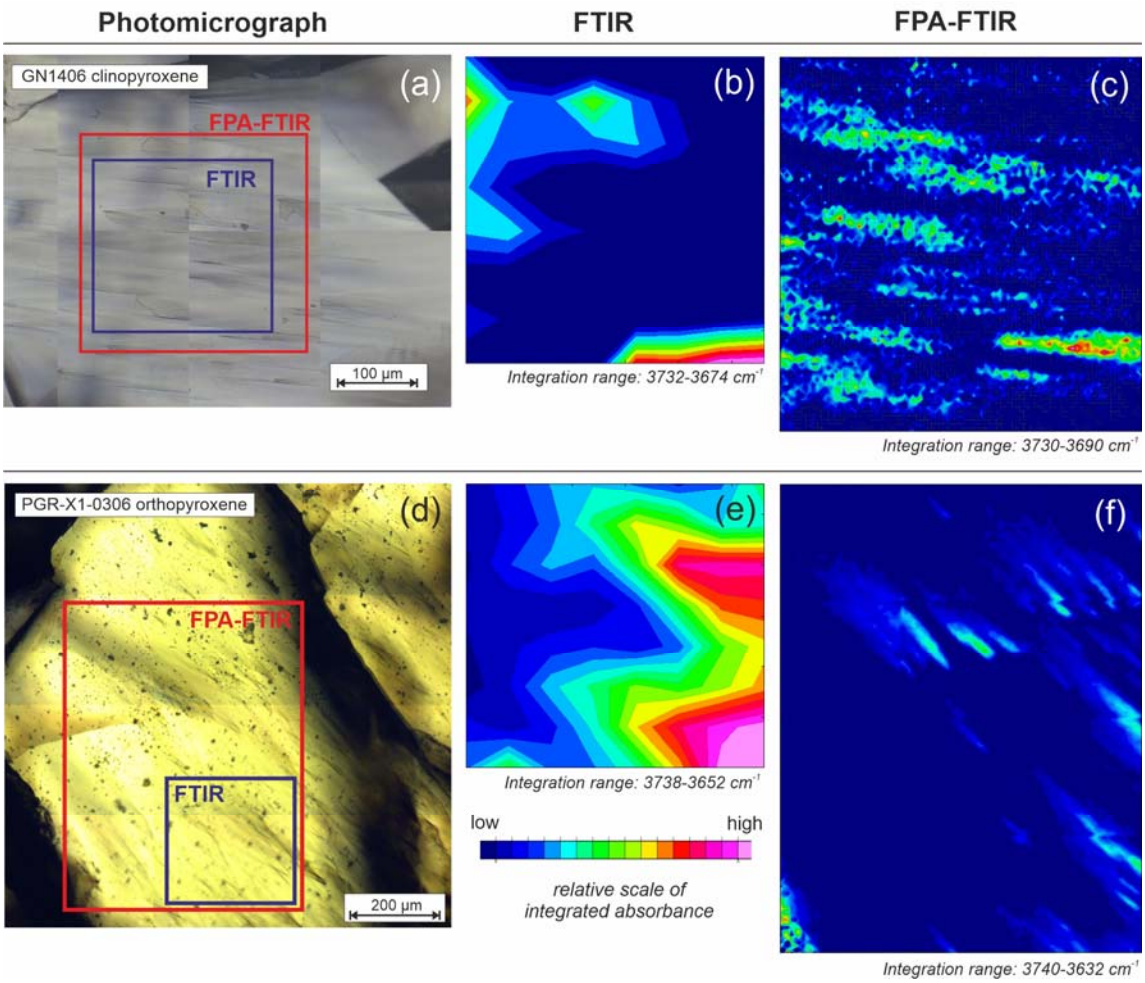

Figure 6. Photomicrographs (transmitted light, 1N) (a, d) and examples of hyperspectral maps carried out with single spot FTIR (b, e) and images generated with a focal plane array (FPA) detector (c, f) on a clinopyroxene (a-c) and orthopyroxene (d-f) from the Styrian Basin and the Perşani Mountains, respectively. Hyperspectral maps and images were constructed from integrated absorbance of the bands characteristic for amphibole.

This is the peer-reviewed, final accepted version for American Mineralogist, published by the Mineralogical Society of America.
The published version is subject to change. Cite as Authors (Year) Title. American Mineralogist, in press.
DOI: https://doi.org/10.2138/am-2022-8662. http://www.minsocam.org/

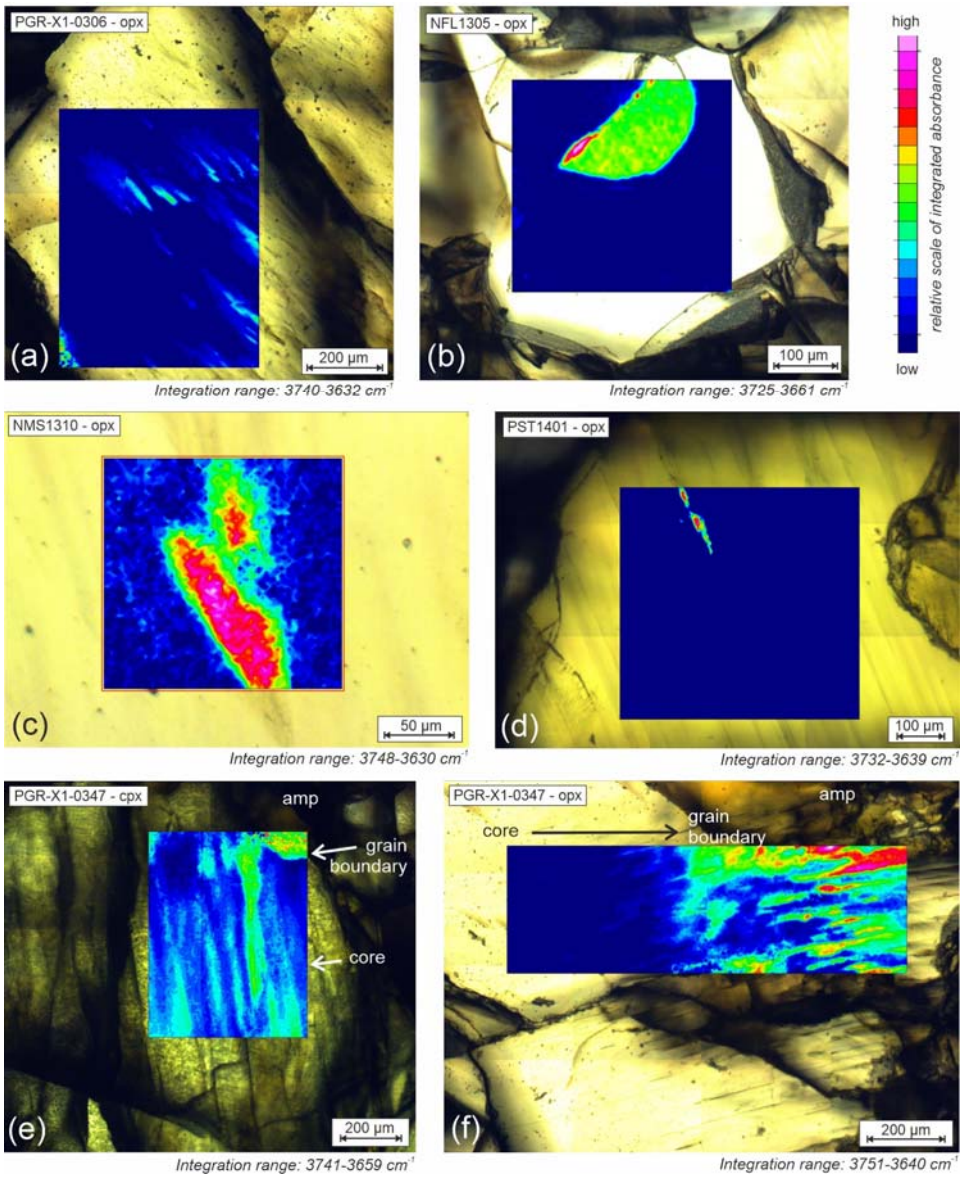

Figure 7. Examples of FPA-FTIR maps displayed over the mapped area on various pyroxene grains from the studied xenoliths. (a) Hydrous lamellae in orthopyroxene. (b) Hydrous phase on the grain boundary between olivine and orthopyroxene. (c-d) Hydrous lamellae in orthopyroxene containing clinopyroxene lamellae as well. (e) Hydrous lamellae in clinopyroxene, connected to a neighboring interstitial amphibole. (f) Hydrous phase in orthopyroxene, connected to a neighboring interstitial amphibole. Note that the color scaling is different for each image, so that the hydrous lamellae are best distinguishable. Integration ranges were chosen based on the shapes of the spectra for best distinction from the signal of the host grain.

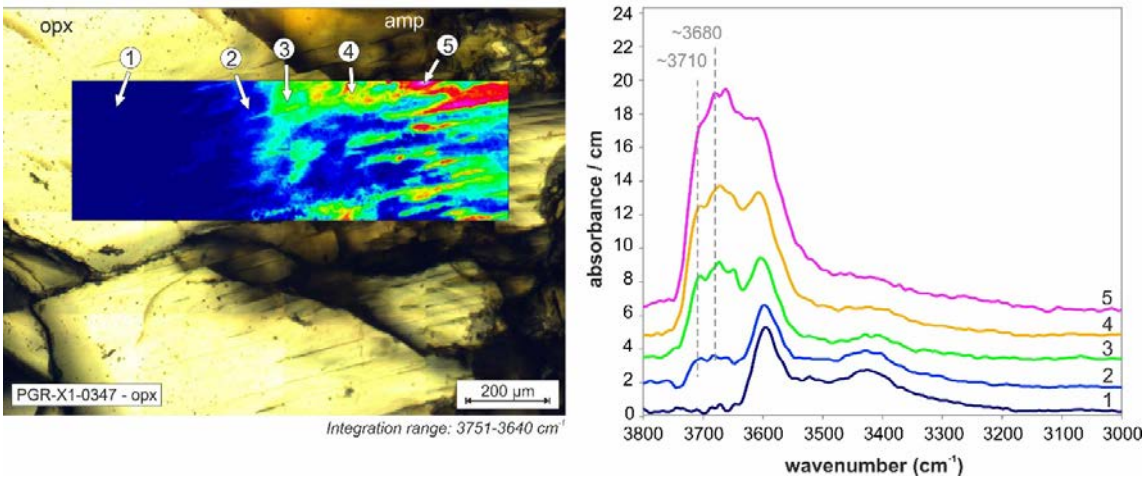

Figure 8. FPA-FTIR hyperspectral map (left) displayed over the mapped area in a Perşani Mountains xenolith (PGR-X1-0347) where amphibole lamellae are in contact with an adjacent interstitial amphibole grain, and FTIR spectra along a profile (right) showing the transition with different proportions of amphibole and orthopyroxene signal. Color scale represents the amount of integrated absorbance similarly as on Fig. 7.

This is the peer-reviewed, final accepted version for American Mineralogist, published by the Mineralogical Society of America.
The published version is subject to change. Cite as Authors (Year) Title. American Mineralogist, in press.
DOI: https://doi.org/10.2138/am-2022-8662. http://www.minsocam.org/

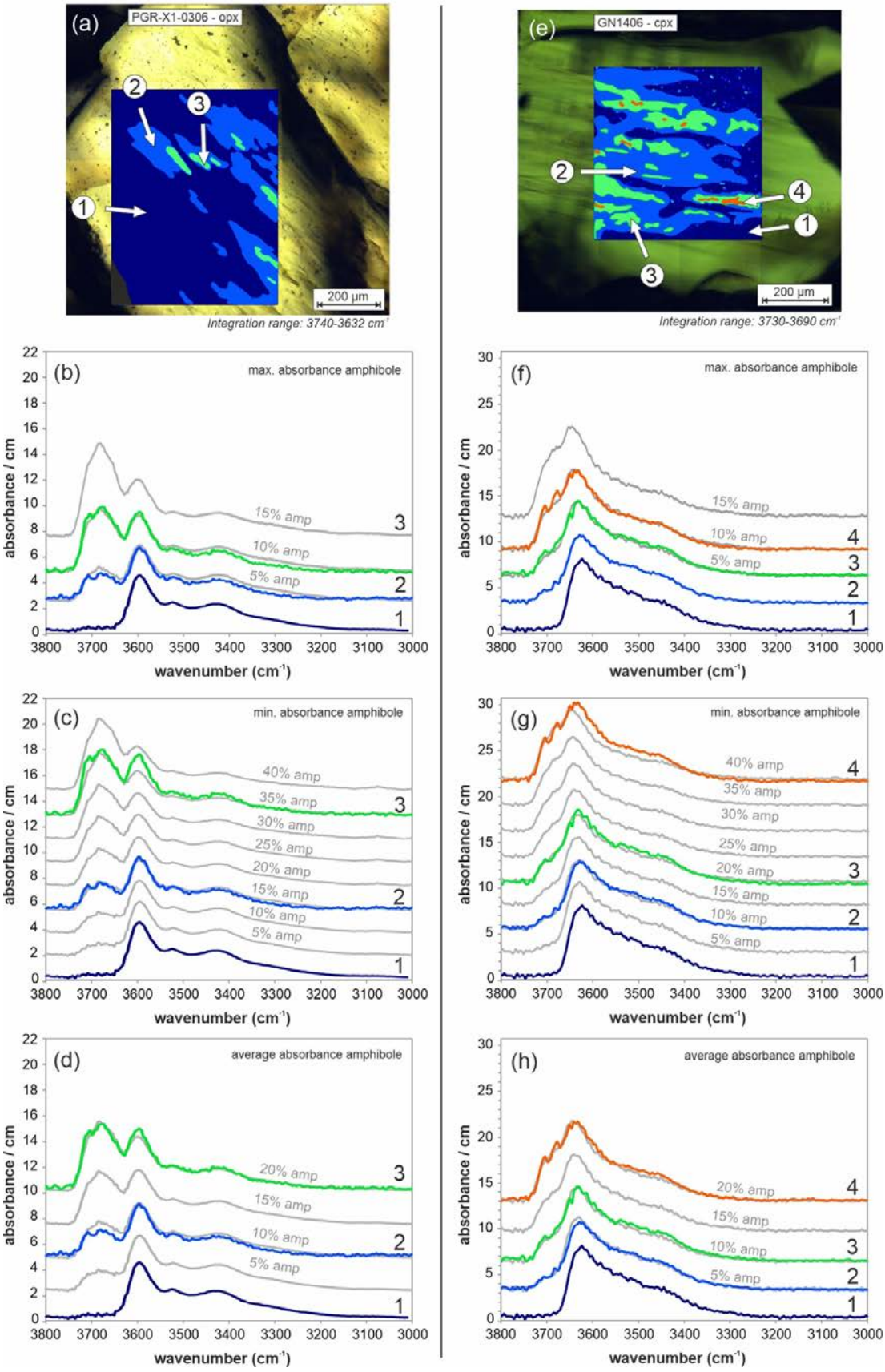

1133

Figure 9. Effect of different volume proportions of amphibole on the infrared spectrum of orthopyroxene (a-d) and clinopyroxene (e-h), same grains as on Fig. 6, by spectrum mixing. Images were re-drawn (a, e) in a simplified way to show areas with 3-4 different amphibole signal intensities in different colors (from dark blue to red). Spectra of amphibole bands with different intensities at the indicated spots are shown in the same colors. Spectrum mixing was carried out with pure amphibole spectra from grain separated from a Perşani Mountains xenolith (see Fig. 4c). For both ortho- and clinopyroxene, the mixing was carried out with the highest (b, f) and lowest (c, g) absorbance amphibole, as well as the averaged (d, h) amphibole spectrum. Total volume proportion of amphibole lamellae and bulk water content in the area covered by the hyperspectral images, extrapolated to the whole grain, were calculated based on fitting with mixed spectra (see text for details).